FOI-R--0814--SE
Feb 2003
1650-1942

Scientific report

Jonathan Smith

Unsteady RANS calculations for the GFSI bump Preliminary study using EURANUS 5.3

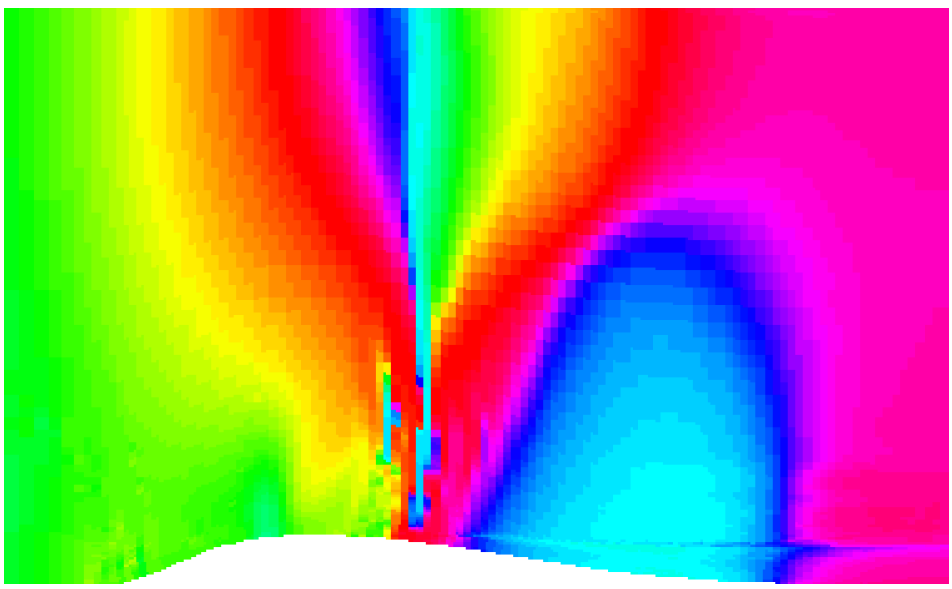

Division of Aeronautics, FFA
SE-172 90 STOCKHOLM

FOI – Swedish Defence Research Agency
Division of Aeronautics, FFA
SE-172 90 STOCKHOLM

FOI-R--0814--SE
Feb 2003
1650-1942

Scientific report

Jonathan Smith

Unsteady RANS calculations for the GFSI bump Preliminary study using EURANUS 5.3

Division of Aeronautics, FFA
SE-172 90 STOCKHOLM

Abstract

Calculations are presented for unsteady transonic flow over an oscillating bump. The flow field is computed using unsteady RANS method using the FFA-developed CFD code EURANUS with the EARSM turbulence model. Flow solutions are presented in the time domain and as Fourier series. The results comprise preliminary predictions for experiments to be carried out at the Department of Energy Technology, KTH, Stockholm.

Contents

List of Figures

1 Introduction

1.1 Background

The 'GFSI bump' is an experimental system which is being studied at the Department of Energy Technology, Heat and Power Division, KTH, Stockholm [1]. The work is part of a project, 'Generic Fluid-Structure Interaction' (GFSI) which is financed mainly by STEM, the Swedish Energy Agency [2]. The experiments will be carried out using the Department's 'VM100' wind tunnel and will measure the unsteady transonic flow over an oscillating bump in the tunnel floor. In this report, we present the results of preliminary CFD calculations providing an initial prediction of the unsteady flow in this system.

This study has been funded by STEM, through a contract with KTH, and by FMV, the Swedish Defence Materiel Administration [3], as part of FOI's long term research in unsteady aerodynamics and aeroelasticity. The support for this work from both FMV and STEM is gratefully acknowledged.

1.2 Experimental System

Figure 1 shows two drawings taken from the CAD model [1] of the GFSI bump: a wind tunnel installation view and a cutaway of the bump. The flexible bump surface is deformed by a rotating camshaft (red) while a flat cavity under the shaft prevents compression of the mounting block (blue). Wind tunnel flow is from left to right. The cam shape is chosen so that, for a constant rotational speed, it produces an exactly sinusoidal displacement of the bump surface.

The bump is oriented perpendicular to the flow and its profile is constant in the transverse direction. The profile resembles the upper half of an aerofoil section, with a smooth convex blending into the wind tunnel floor at the leading and trailing edges. The bump has a streamwise length of 20 cm and a peak height of 1 cm. The amplitude of the surface displacement due to the cam motion is about 0.5 mm. The leading and trailing edges are sealed but there will be a small gap between the bump and the tunnel side walls to allow unrestricted movement.

The experimental system is designed to provide a moving boundary with an exact prescribed motion. Mechanical properties are chosen to eliminate any aeroelastic interaction with the flow. The bump should have a constant displacement profile over a wide range of camshaft speeds. To achieve this, its vibrational modes must have natural frequencies significantly higher than the maximum driving frequency, which is around 600 Hz. If these criteria are satisfied then any deflection of the moving surface due to the fluid loads should be negligibly small.

Measurements will be made of the time-dependent surface pressure distribution, using a built-in array of *Kulite* transducers. A sparser array of accelerometers will allow the shape of the moving bump to be monitored. An independent series of measurements, using a laser-Doppler technique, will provide a more detailed description of the oscillating surface shape at the selected test frequencies. The flow field above the surface will be investigated using Schlieren optics.

[1] Images supplied by Davy Allegret-Bourdon, Department of Energy Technology, KTH.

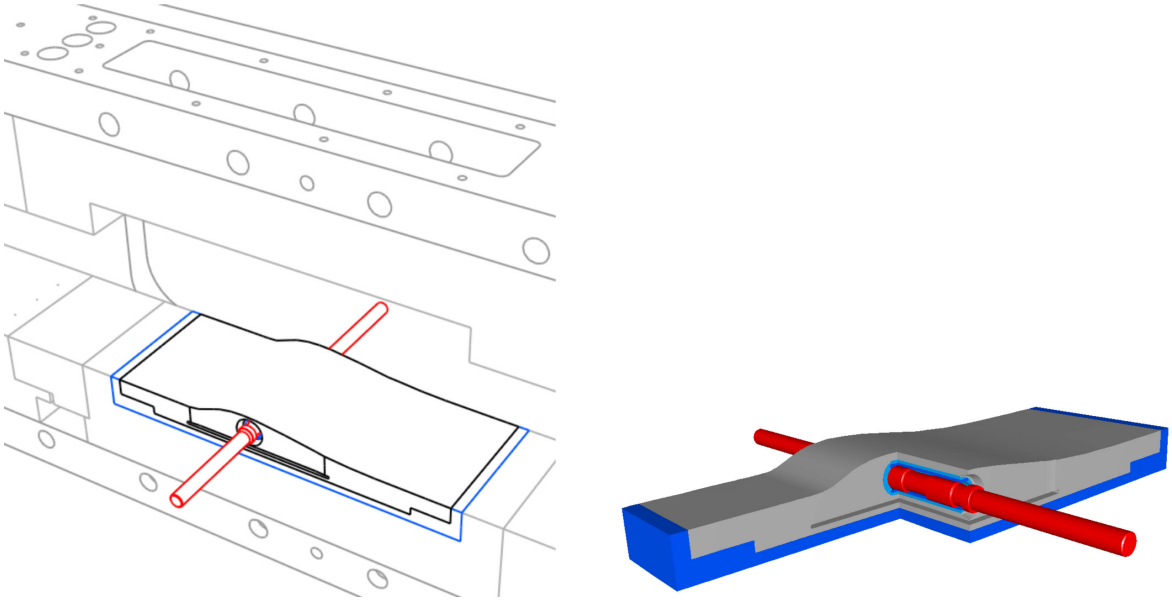

Figure 1. CAD drawings of the GFSI moving-bump system.

1.3 Computational Objectives

The main focus of the experimental programme will be on the time dependent properties of the flow at, or near, the bump surface. The most detailed measurements will be made in the central vertical plane of the flow and along the centreline of the bump surface. It is therefore reasonable to reduce the CFD model to a two dimensional slice in the central plane. This simplification makes it possible to use an Unsteady RANS [2] method, at a relatively low computational cost.

The mechanical properties of the bump are such that aeroelastic effects are negligible. The system can therefore be modelled as channel flow with one boundary subject to an oscillatory prescribed motion. The bump motion is small, so the resulting flow can be treated as periodic oscillation about a mean field similar to the steady solution. The unsteady flow can thus be represented as a Fourier series, with a fundamental frequency equal to that of the prescribed surface oscillation.

At the time of writing, no information was available on the mechanical properties of the experimental system. It has therefore been necessary to use an assumed shape for the bump surface deflection. Whilst the driving frequency is continuously variable, only three cases are considered here: 10 Hz, 100 Hz and 500 Hz.

[2] Reynolds Averaged Navier Stokes

2 Computational Procedure

2.1 Flow Computation

EURANUS All flow computations presented here were carried out using the FFA-developed CFD code EURANUS [4], a fully-featured multiblock solver. Here the EURANUS code is used in unsteady RANS mode, with a single moving boundary and deforming mesh. For such applications, it is necessary to use a numerical scheme which ensures that the flow solution is not polluted by the mesh motion. This is usually formulated in terms of the so-called 'Geometric Conservation Law' (GCL). In EURANUS, compliance with the GCL is achieved using a Volume Discharge method [5].

The unsteady flow field is computed using a dual-timestepping unsteady RANS scheme. Dual timestepping, as introduced by Jameson [6], time-marches the solution through a series of fixed 'real' timesteps, at each of which the flow field is updated in a 'pseudo time' inner loop of iterations. The inner loop runs as for a steady solution, using the same convergence acceleration techniques. This allows the 'real' timestep to be selected without compromising the stability of the solution. The calculations presented here use either 50 or 100 timesteps per period of the surface oscillation. Unsteady solutions for the moving bump are initialised with a fully-converged steady solution.

In an unsteady RANS computation, the solution is resolved in space and time at the scales set by the primary grid and the real timestep. Everything else is handled by a turbulence model. A variety of turbulence models are available in EURANUS. In this study we use an Explicit Algebraic Reynolds Stress Model, the Wallin and Johansson EARSM [7].

Hardware All EURANUS computations were run serially on a single processor of the FFA Compaq GS60 cluster. Post-processing operations were carried out using a Pentium III Linux PC.

Computational Mesh The two-dimensional grid used for the steady CFD calculation is shown in figure 2. The top view shows the whole computational domain whilst the middle view shows the 'working section' grid around the bump. The mesh resolution is refined in the upper and lower wall regions to ensure adequate resolution of the boundary layer flow. This is shown in detail in the trailing edge detail view. The computational mesh is a single block, comprising two such planar grids separated by 0.01 m.

Mesh Movement In EURANUS, mesh deformation is handled using linear combination of a predefined set of 'perturbation grids', a procedure suited to modal coupled aeroelastic solutions. The GFSI bump is modelled as a single mode system, with an assumed boundary displacement as shown in figure 3. The maximum displacement is 0.489 mm, directly over the camshaft axis. A single perturbation grid corresponding to the maximum displacement position was constructed from the base mesh using a transfinite interpolation procedure [8] implemented in the program FFANET [9]. The position vector, $\mathbf{X}$, of any node in

the mesh is given in terms of a single generalised coordinate $q(t)$ such that

$$\mathbf{X}(t) = \mathbf{X_0} + q(t)\big(\mathbf{X_1} - \mathbf{X_0}\big) \quad (1)$$

$$q(t) = \frac{1}{2}\left(1 - \cos\omega t\right) \quad (2)$$

where the subscripts 0 and 1 denote respectively the base mesh and the perturbed mesh and ω is the angular frequency of the bump surface oscillation. The form of $q(t)$ is chosen to ensure continuity with the initial steady solution at $t = 0$.

Boundary Conditions The boundary conditions applied are summarised in table 1. The entries for 'Boundary Type' and 'Identifier' are defined fully in the EURANUS User Guide [4]. External boundaries are defined for the inlet and outlet planes. At the inlet boundary, the velocity, static pressure, temperature and the turbulent fields, K and ω, are fixed and the total pressure is extrapolated from the interior. At the outlet boundary, a constant back pressure is imposed, with all other variables extrapolated from the interior. For the floor and ceiling ($\mathrm{y} = 0.12\,\mathrm{m}$) boundaries, an adiabatic wall condition is applied so that the boundary layer is resolved for the whole length of the domain. An Euler wall condition is used for the four-cell layer nearest the inlet boundary but this is simply to avoid a known inconsistency in combining the inlet and wall boundary conditions and has negligible effect on the solution. Mirror conditions are imposed at the bounding planes, $\mathrm{z} = 0$ and $\mathrm{z} = 0.01\,\mathrm{m}$. The boundary data is given in table 2, where derived quantities are denoted by italic type. The data values are for the Mach 0.7 design point of the VM100 tunnel.

Table 1. Boundary Conditions

Boundary Type	Identifier	Location
external	inlet_pextr	$\mathrm{x} = -0.2500\mathrm{m}$: inlet
external	back_pressure	$\mathrm{x} = +0.6300\mathrm{m}$: outlet
wall	Euler_pgr	$0.0000\mathrm{m} \leq \mathrm{x} \leq -0.2428\mathrm{m}$: floor & ceiling
wall	adiabatic	$-0.2428\mathrm{m} < \mathrm{x} \leq 0.6300\mathrm{m}$: floor & ceiling
boundary	mirror	$\mathrm{z} = 0.0000\mathrm{m}, \quad \mathrm{z} = 0.0100\mathrm{m}$

Table 2. Boundary Data

Boundary Data			
Static Pressure	P_0	1.15823e5	$\mathrm{N\,m^{-2}}$
Temperature	T_0	302.4	K
Velocity	U	244.0	$\mathrm{m\,s^{-1}}$
	V	0	$\mathrm{m\,s^{-1}}$
Mach	M	0.7	
Turbulent-			
-Energy	K	3.1383	$\mathrm{m^2 s^{-2}}$
-Omega	ω	1640.3	$\mathrm{s^{-1}}$
-Dissipation	ϵ	463.31	$\mathrm{m^2 s^{-2}}$
-*Viscosity*	μ_T	2.6e-3	$\mathrm{kg\,m^{-1} s^{-1}}$
-*Length*	L_T	1.6	m
Outlet			
Back Pressure	P_B	1.09442e4	$\mathrm{N\,m^{-2}}$

Reduced Frequency The reduced frequency is here defined as

$$\nu = \frac{fL}{U_0} \tag{3}$$

where f is the frequency of the surface oscillation, $L = 0.20\,\mathrm{m}$, is the streamwise length of the bump and U_0 is the free stream velocity as given in table 2. The reduced frequency, ν, is the ratio of the free stream surface transit time to the period of oscillation. Conversely, the quantity, ν^{-1}, or 'reduced wavelength', represents the distance travelled by the free stream per period in units of L. Values of ν and ν^{-1} for the three frequency cases considered here are given in table 3.

Table 3. Reduced Frequency

Hz	ν	ν^{-1}
10	0.0082	122.00
100	0.0820	12.20
500	0.4098	2.44

2.2 Post-processing and Analysis

Post-processing and analysis of the steady and unsteady solutions was carried out using programs based on the 'FFA Matlab Toolbox' [10]. These were used both for data display and to resolve the unsteady fields into Fourier series components. All field plots are presented without spatial smoothing, so that each colour element corresponds to a single cell in the grid.

For the Fourier analysis, it is assumed that the flow field is a periodic function of time with a fundamental frequency, $f = \frac{1}{T}$, equal that of the surface deflection. Let $p(t)$ denote the value of any one of the scalar fields at a given point in the mesh. The Fourier series expansion for $p(t)$ is defined as

$$p(t) = \frac{C_0}{2} + \sum_{n=1}^{\infty} |C_n| \cos\left(n\omega t - \phi_n\right) \tag{4}$$

$$= \frac{a_0}{2} + \sum_{n=1}^{\infty} \left(a_n \cos\left(n\omega t\right) + b_n \sin\left(n\omega t\right)\right) \tag{5}$$

where $\omega = \frac{2\pi}{T}$, is the angular frequency of the surface oscillation. The complex coefficients, C_n, are given by

$$C_n = \frac{2}{T}\int_{t_1}^{t_1+T} e^{in\omega t} p(t)\,\mathrm{d}t \tag{6}$$

in which T, is the period of oscillation and t_1, is an arbitrary time. The real coefficients, a_n and b_n, and phase angles, ϕ_n, are given by

$$\phi_n = \tan^{-1}\left(\frac{b_n}{a_n}\right); \qquad \left.\begin{array}{rcl} a_n &=& \mathrm{Re}\left[C_n\right] \\ b_n &=& \mathrm{Im}\left[C_n\right] \end{array}\right\} \tag{7}$$

By applying the same transformation at all mesh points, the solution is resolved into a series of complex 'harmonic fields', corresponding to the coefficients, C_n. Taking the real and imaginary parts or using a phase-magnitude representation, these fields can be displayed using the same techniques as for a steady solution. Results from such an analysis are presented in section 3.

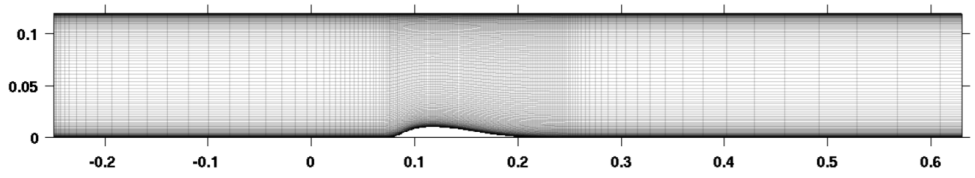

Whole Domain

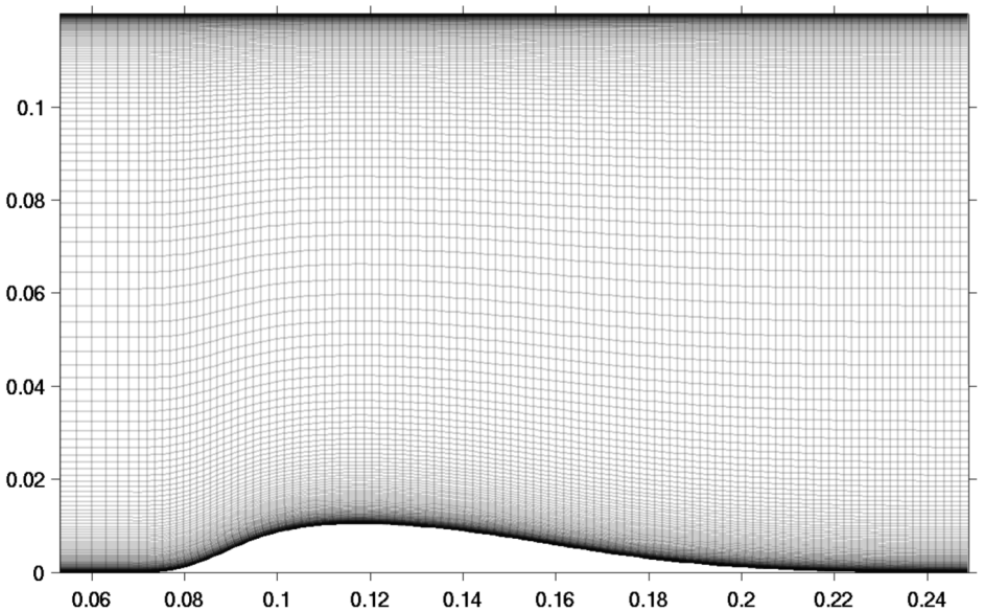

Working Section

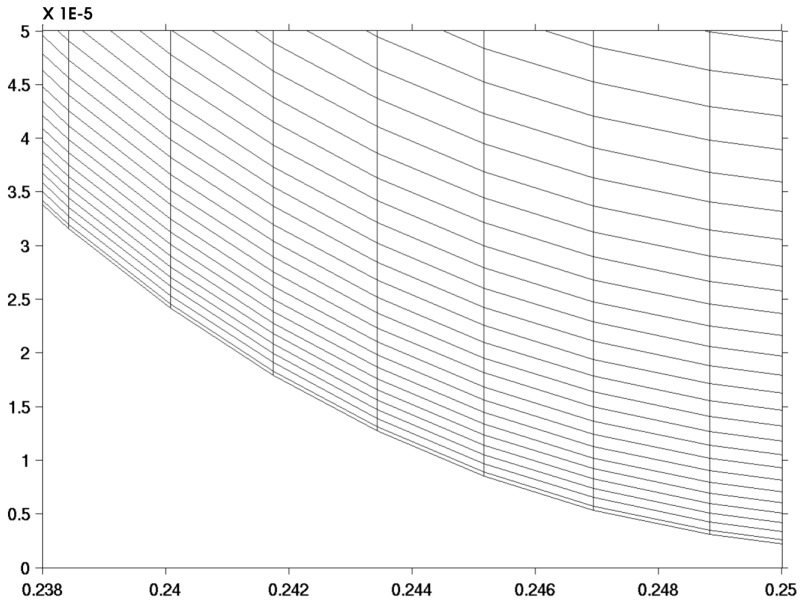

Trailing Edge Detail

Figure 2. CFD computational grid (dimensions in metres)

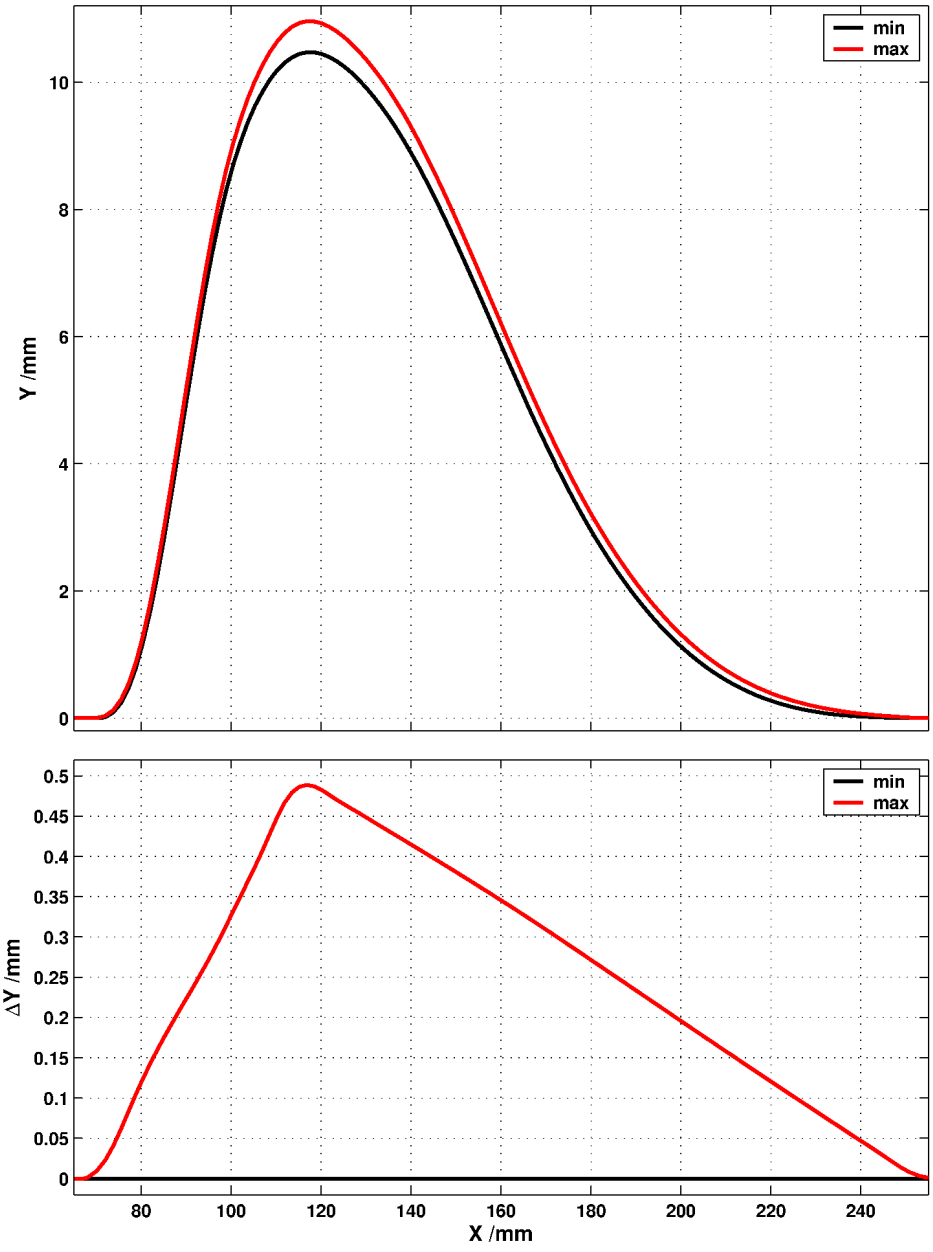

Figure 3. Bump profile position and displacement limits

3 Results

3.1 Steady Solution

All results are given in SI units, with the turbulence variables as presented in table 2

The steady solution was generated for zero surface deflection, with the initial free stream set to the boundary values given in table 2. The resulting Mach number distribution is shown for the full domain in figure 4. Most of the flow is close to the specified, Mach 0.7, free stream condition. In the vicinity of the bump peak, the flow is accelerated resulting in a small transonic region.

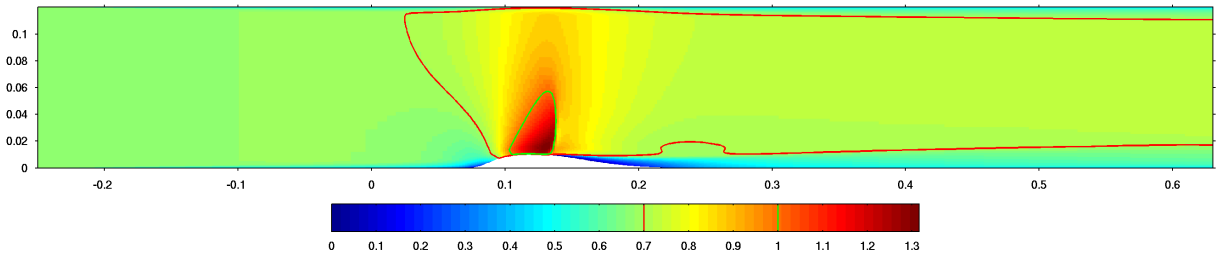

Figure 4. Steady Solution: Mach: Full Domain

The solution is shown in detail for the ‘working section’ region in figure 5. The Mach and Pressure displays indicate a roughly triangular region of transonic flow bounded by a shock which meets the bump surface at $x \approx 0.135\,\mathrm{m}$.

The $U = 0$ contour in the velocity field reveals a small separation bubble in the surface region, $0.133\,\mathrm{m} \leq x \leq 0.147\,\mathrm{m}$. The separation generates a sharply defined wake in the turbulent energy and increased turbulent viscosity in the downwind boundary layer.

The turbulent viscosity shows evidence of a ‘source and wake’ structure starting in the shock at about $y = 0.03\,\mathrm{m}$. This appears to arise from the shear due to the extreme velocity gradient in this region. However, from these results alone, it is not possible to say whether this represents the correct physical behaviour, or is merely a numerical artefact.

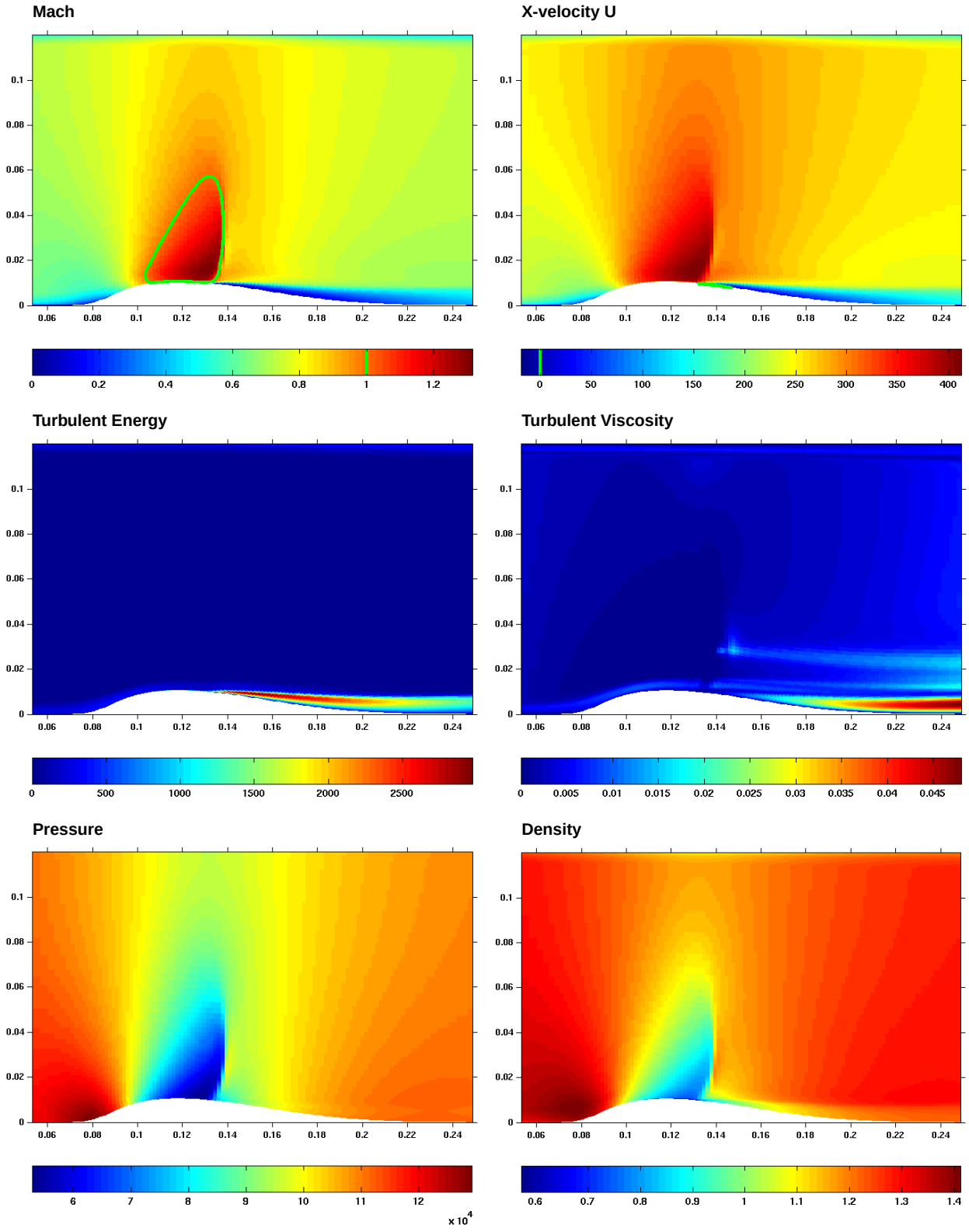

Figure 5. Steady Solution: Working Section

3.2 Oscillatory Solutions

3.2.1 Cyclic Convergence

The three unsteady solutions were all computed using a constant, and probably excessive, 40 inner iterations. The 100 Hz case was computed first, using 100 timesteps per period. The elapsed time for this was about 15 minutes per timestep, so for the remaining cases the resolution was reduced to 50 timesteps per period. The convergence of the oscillatory solution was identified by monitoring the 'cyclic residual' of the global drag coefficient, $D(t)$, given by

$$\Delta D(t) = D(t) - D(t - T) \tag{8}$$

where T is the period of surface oscillation. Convergence histories for the three frequency cases are shown in figures 6, 7 and 8. Each figure shows the time evolution of the generalised coordinate, q, drag, D, and cyclic residual $|\Delta D|$ together with a cross-plot of $D(t)$ and $q(t)$. For each of the three solutions, a single period of oscillation was selected for analysis: the interval starting with $q = 0$, with the lowest mean value of $|\Delta D|$. For the cases 10, 100 and 500 Hz, these were respectively periods 5, 9 and 8 of the oscillation. Note that this procedure is based on a global integral of surface forces. Even if this quantity is cyclically converged, the same may not be true for local values at some points in the flow.

3.2.2 Surface Pressure: Time Domain

The surface pressure distribution is shown as a function of time in figures 9 to 11. In each of these figures, the oscillatory component of the surface pressure is shown as a colour contour map with the time axis vertical. The colour scale shows zero oscillatory pressure as green and a 'lifting' pressure as blue. The generalised coordinate $q(t)$ is plotted on the same time axis. Below the map, are shown the mean pressure distribution and the bump profile. Each figure shows a single cycle of oscillation, with the top and bottom of the pressure map corresponding to equivalent, zero displacement, positions. Pressure values are in $\mathrm{N\,m^{-2}}$.

The mean pressure distributions are all very closely similar, with a smooth drop in the pressure from the leading edge up to the shock position, at $x \approx 0.135\,\mathrm{m}$. These results are similar to the steady solution. The oscillatory pressure has roughly the same peak magnitude for all three frequencies, 3 kPa for the 10 Hz and 100 Hz cases and about half that value at 500 Hz. For all three cases, the surface pressure response is predominantly at the same frequency as the surface oscillation, with no visible evidence of 'drift', or of any higher frequency fluctuations. The spatial distribution and phasing of the oscillatory pressure shows marked variation between the three cases. For example, at 10 Hz and 500 Hz, the 'positive lift' minimum in the pressure coincides with maximum surface displacement. For the 100 Hz case however, the pressure minimum occurs when the surface has maximum downward velocity.

3.2.3 Surface Pressure: Fourier Analysis

Figures 12 to 14. show the results of Fourier analysis using the same surface pressure data as presented in section 3.2.2. Each figure shows, as real and imaginary

parts, the first five Fourier components of the oscillatory surface pressure distribution, as defined in equation 5. The series includes the 'zeroth harmonic' term, $\frac{a_0}{2}$, which is the same time averaged pressure as shown in figures 9 to 11.

For all three cases, at all multiples of the driving frequency, the response peaks near the mean shock position at $x \approx 0.135\,\mathrm{m}$ and the fundamental, $n = 1$, component is about an order of magnitude stronger than the sum of the higher harmonics. In the $n = 1$ component, near the shock position, the response at 10 Hz is mostly in the real part, whereas for the 100 Hz case the imaginary part is strongest. These observations are all consistent with the behaviour shown in the time domain results of section 3.2.2.

For the 10 Hz case, the response in the higher harmonics, $n \geq 2$, is almost zero upwind of the bump peak at $x = 0.1168\,\mathrm{m}$. Similar behaviour is observed for the 100 Hz case, up to $n = 3$ (300 Hz) but at all higher frequencies, including the 500 Hz case, there is no such 'upwind cut off' effect. This suggests the existence of a frequency threshold for the propagation of surface pressure fluctuations, somewhere between 300 and 400 Hz (reduced frequency: $0.25 \leq \nu \leq 0.33$). However, more detailed calculations would be required to confirm this.

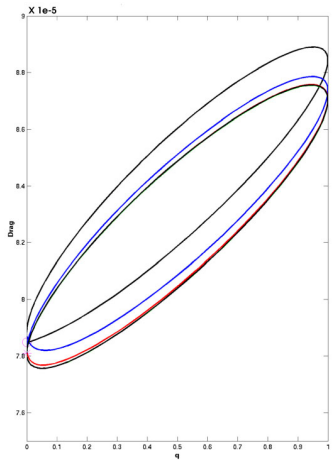

DRAG vs DISPLACEMENT

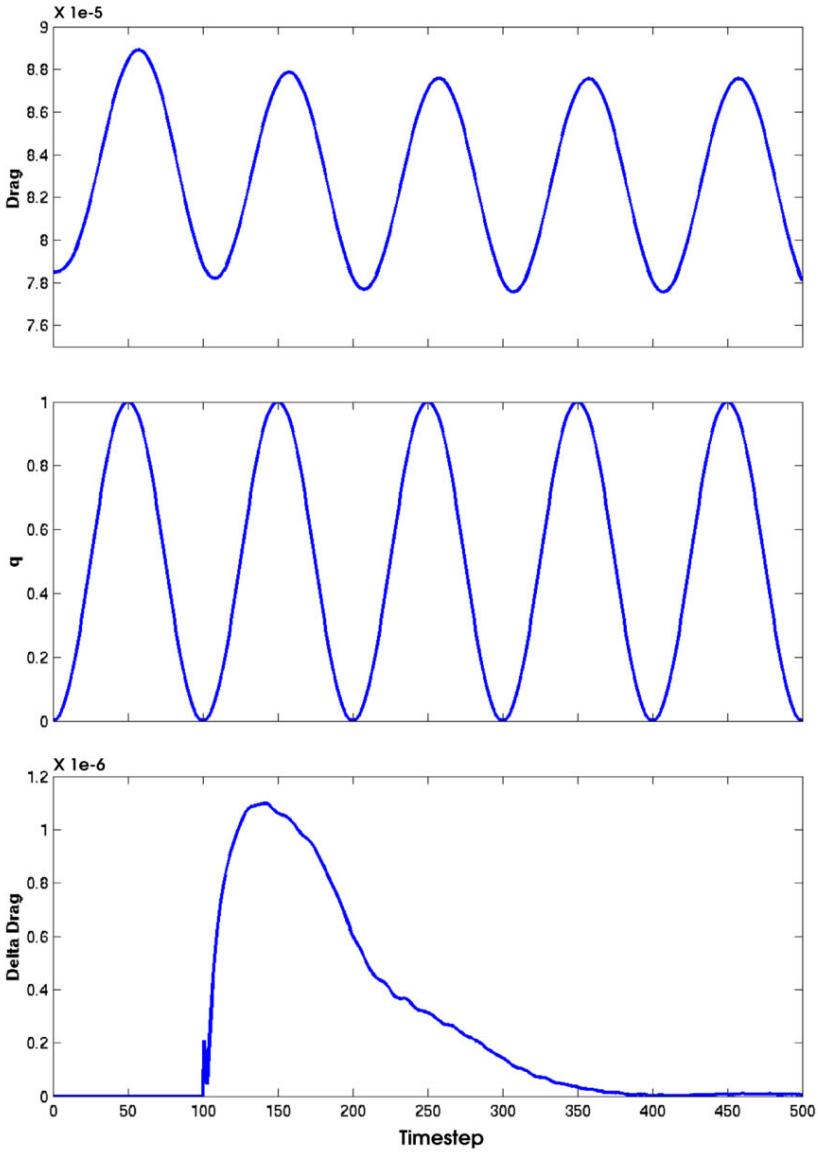

DRAG / DISPLACEMENT / CYCLIC-RESIDUAL vs TIMESTEP

Figure 6. Cyclic convergence history: 10 Hz

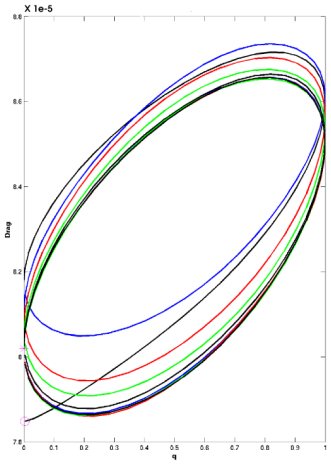

DRAG vs DISPLACEMENT

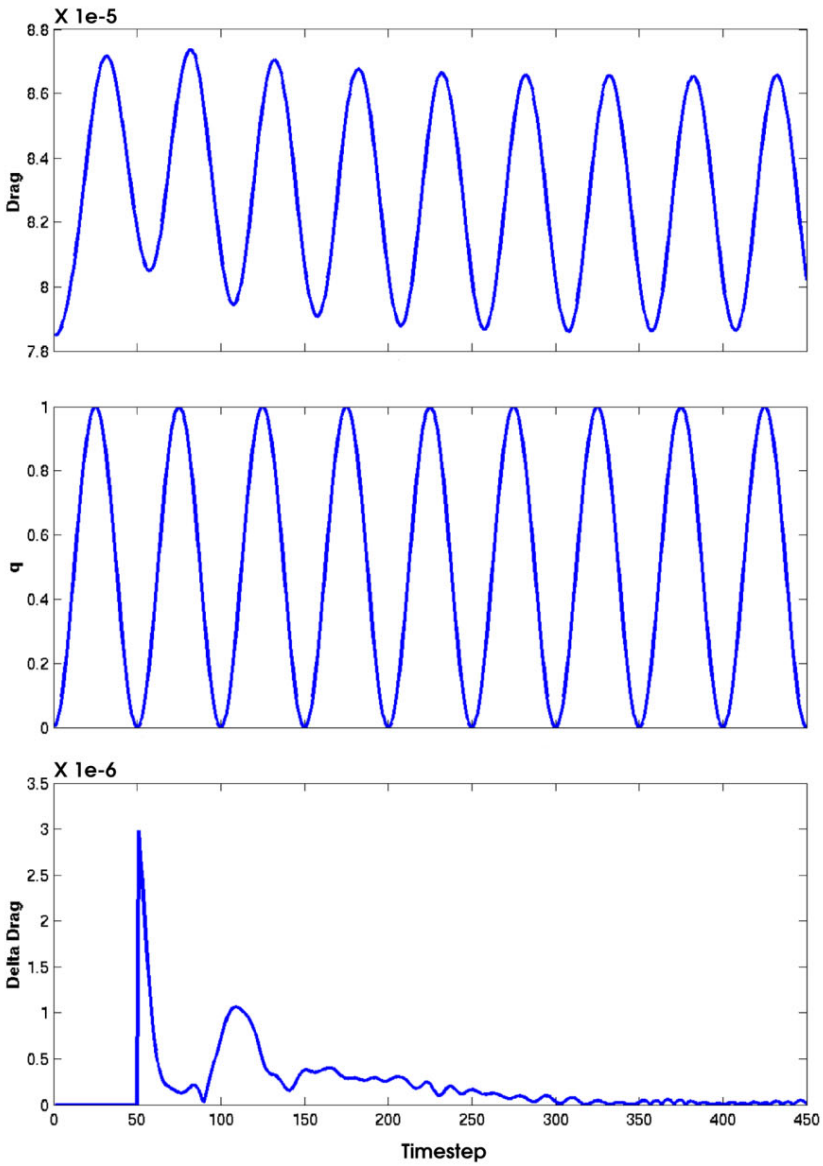

DRAG / DISPLACEMENT / CYCLIC-RESIDUAL vs TIMESTEP

Figure 7. Cyclic convergence history: 100 Hz

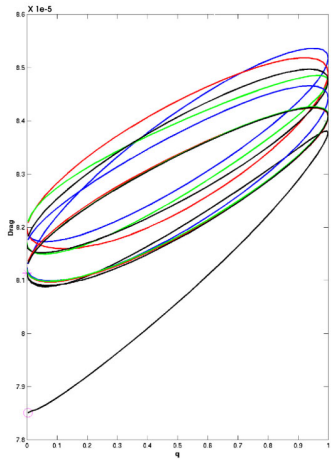

DRAG vs DISPLACEMENT

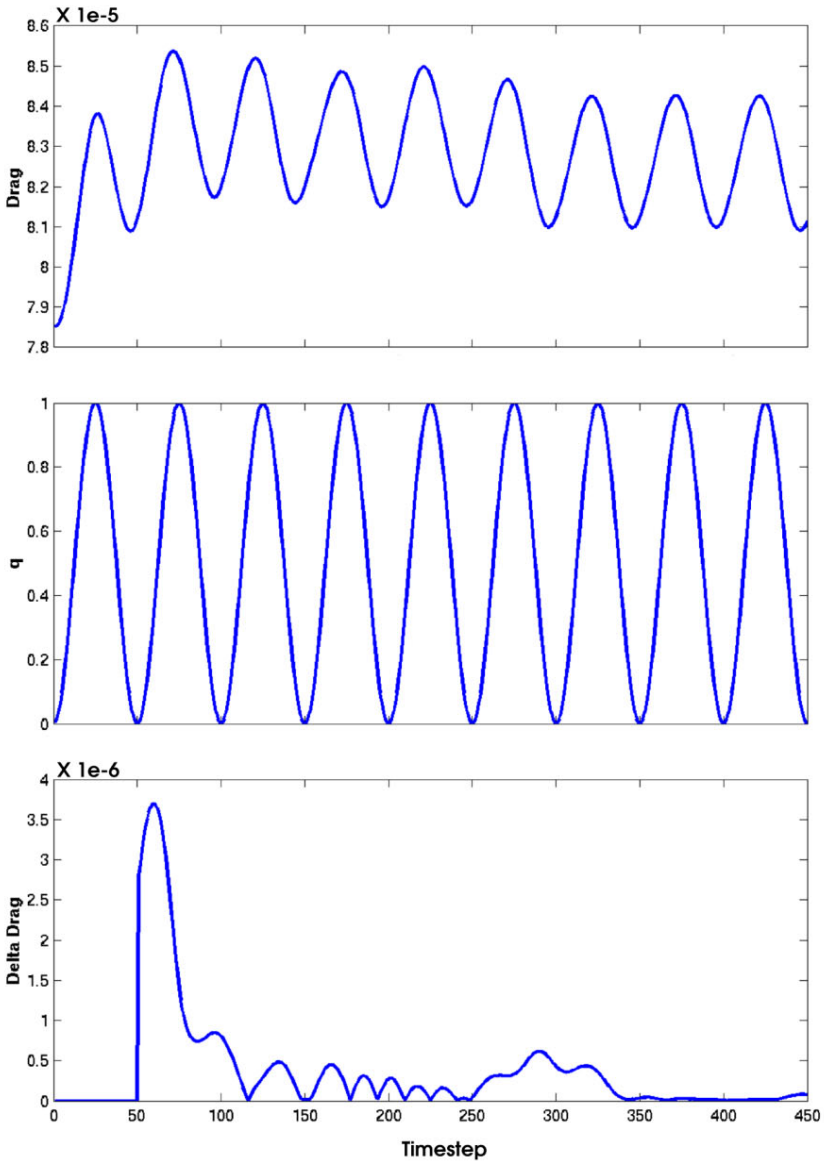

DRAG / DISPLACEMENT / CYCLIC-RESIDUAL vs TIMESTEP

Figure 8. Cyclic convergence history: 500 Hz

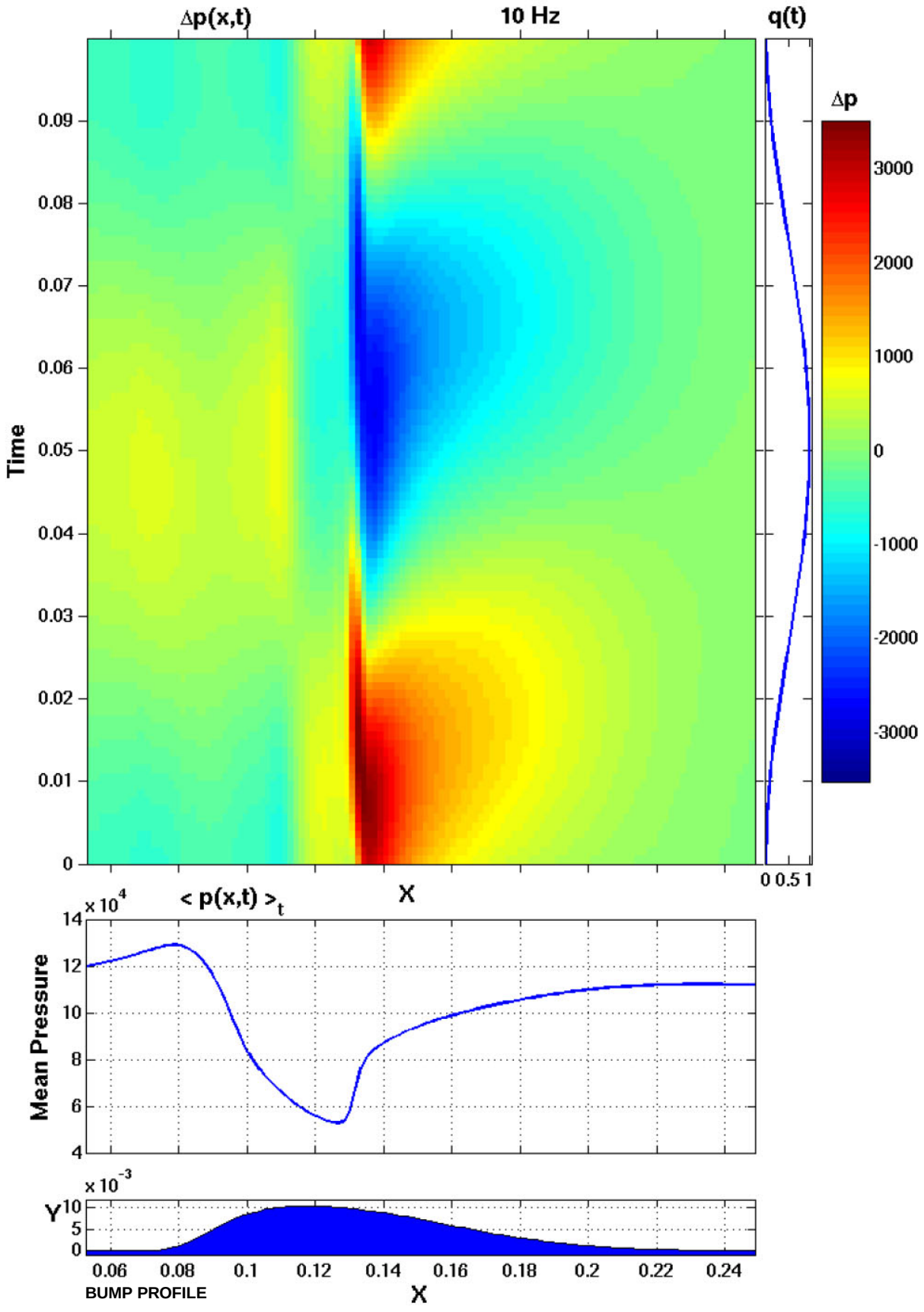

Figure 9. Time evolution of surface pressure: 10 Hz

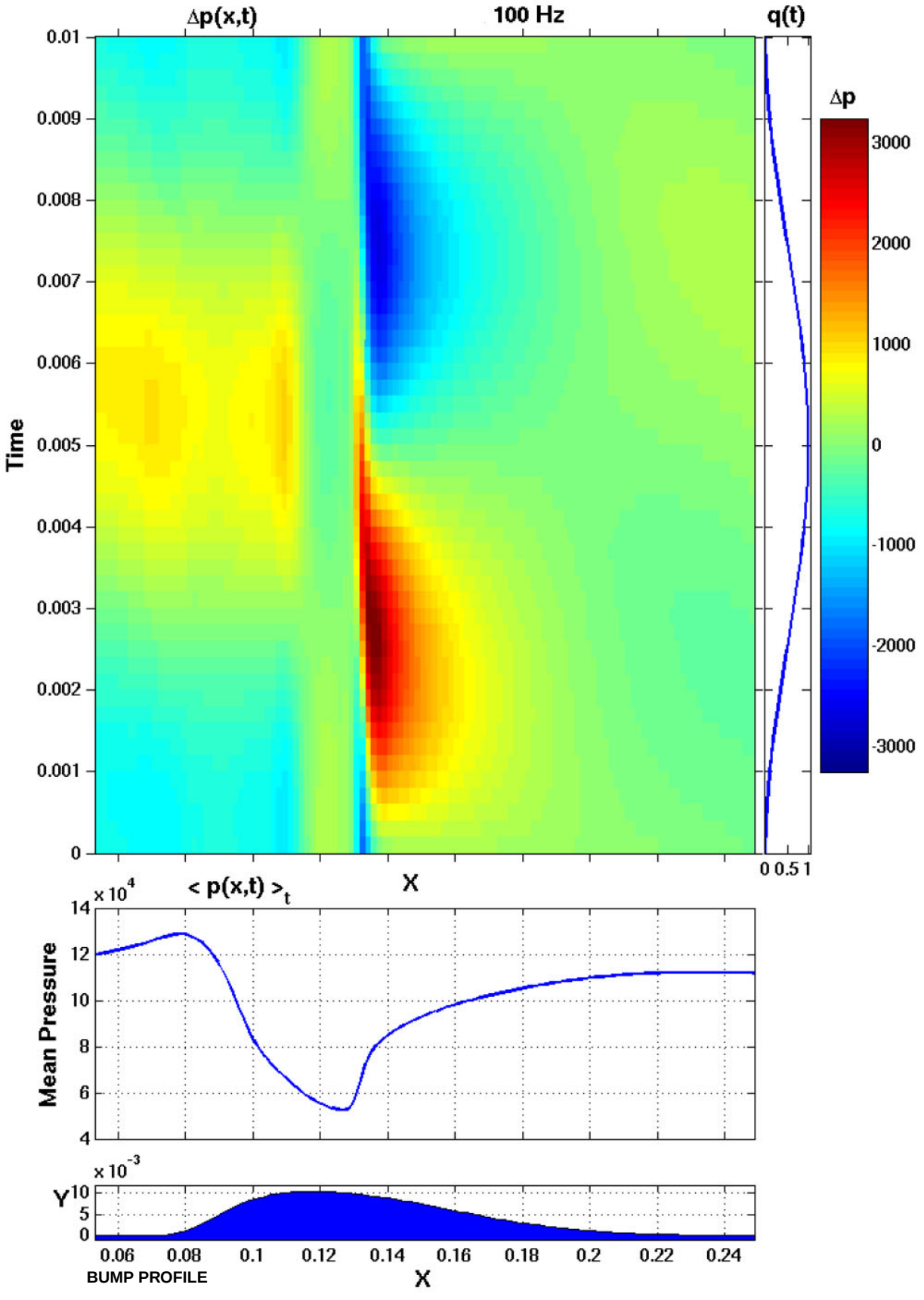

Figure 10. Time evolution of surface pressure: 100 Hz

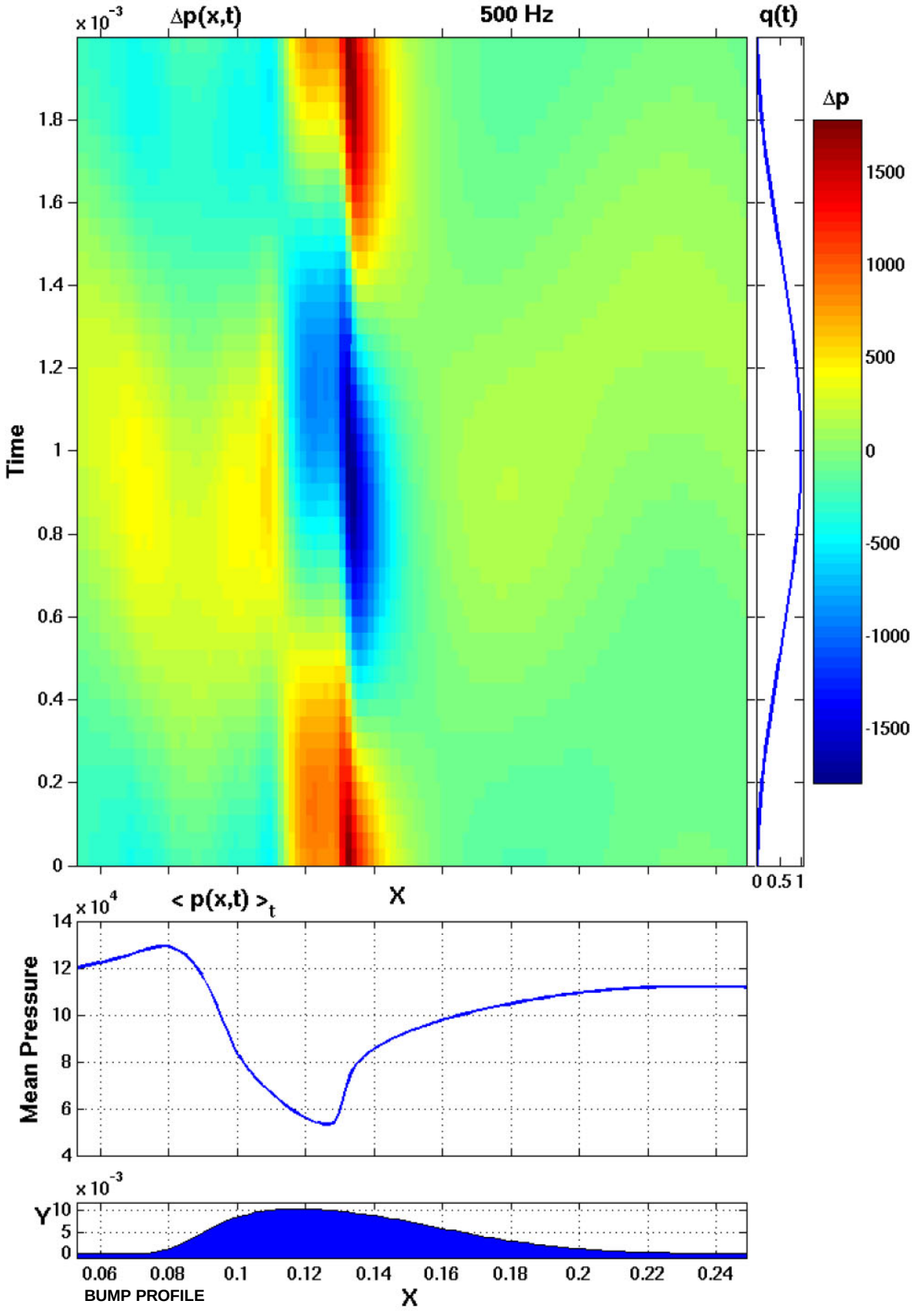

Figure 11. Time evolution of surface pressure: 500 Hz

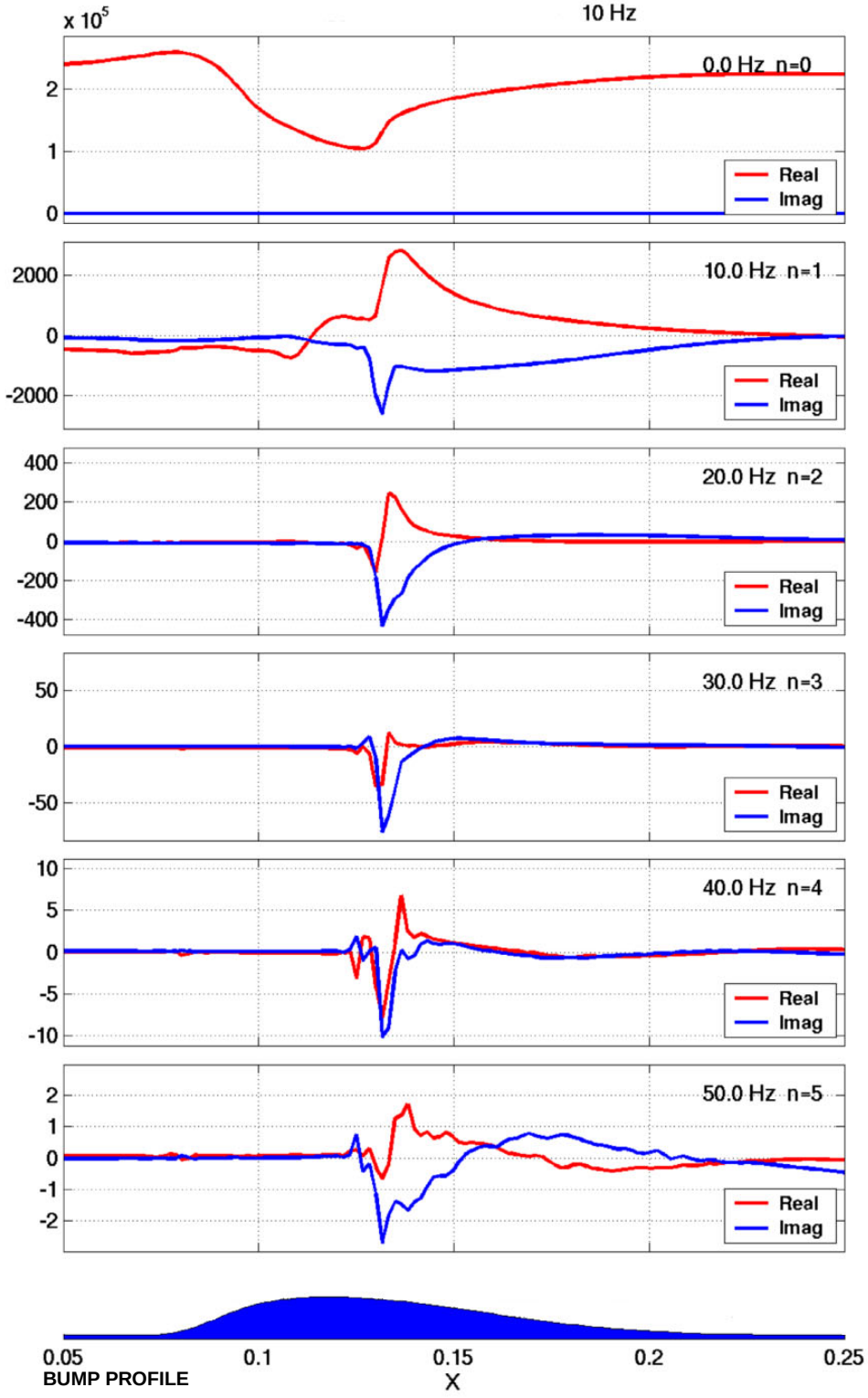

Figure 12. Fourier Surface Pressures: 10 Hz

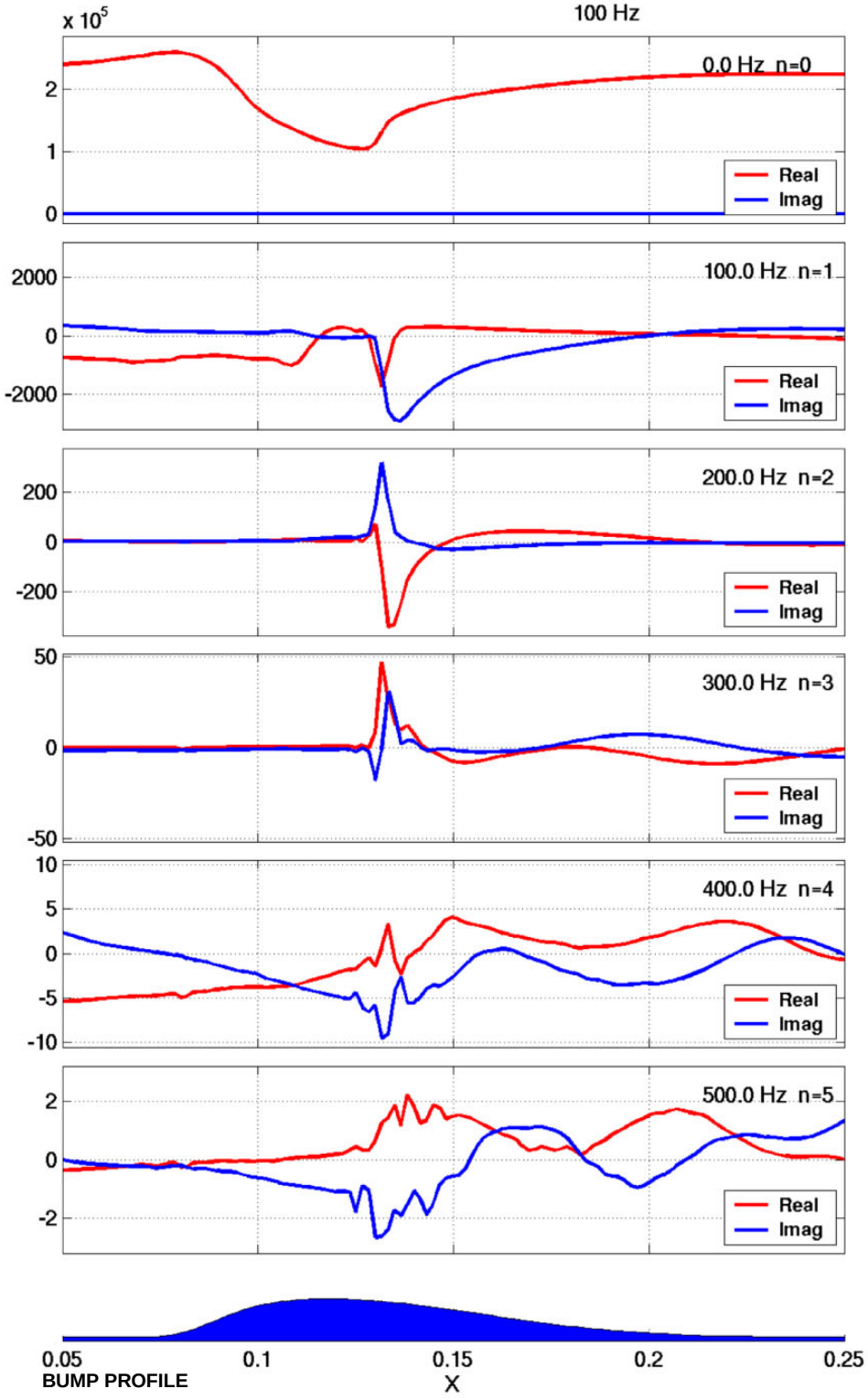

Figure 13. Fourier Surface Pressures: 100 Hz

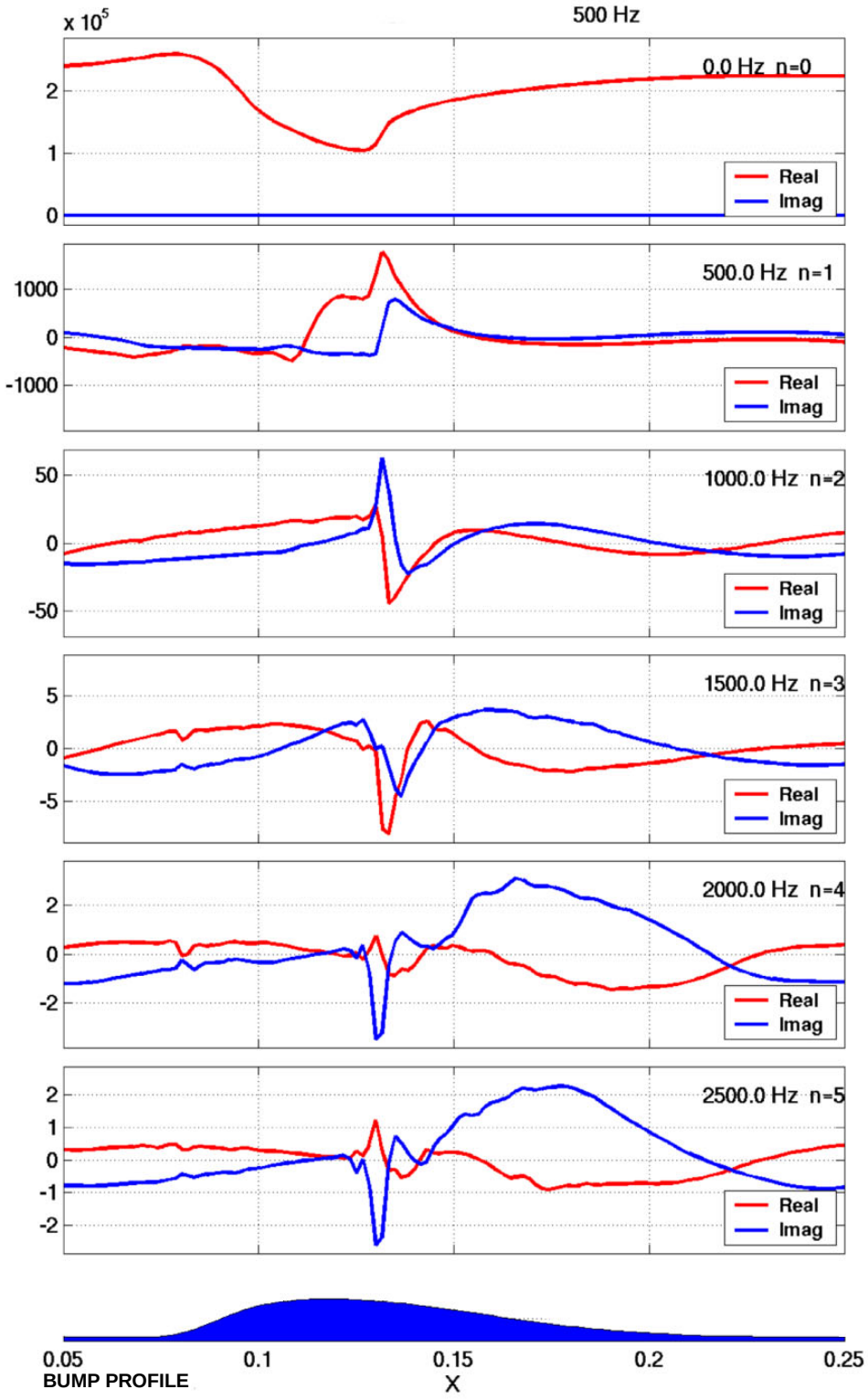

Figure 14. Fourier Surface Pressures: 500 Hz

3.2.4 Field Variables: Time Domain

The only way to display a two dimensional field in the time domain is as a sequence of animation frames. This makes it impractical to display as many field variables as for a steady solution. Attention is therefore restricted to the pressure and turbulent energy, since these reveal both the shock structure and the turbulent wake from the separation bubble.

To display the oscillatory component of any of the flow variables it is necessary, as in section 3.2.2, to subtract the time averaged field. Figure 15 shows the difference between the time averaged and steady solution fields. All three frequency cases have closely similar behaviour. Pressure changes are largely confined to the shock, where there is drop of up to 10 kPa above $y \approx 0.02\,\mathrm{m}$, with a smaller increase in pressure near the bump surface. The turbulent energy in the wake is increased by up to $10^3\,\mathrm{m^2 s^{-2}}$. Referring to figure 5, it can be seen that these changes are consistent with a downwind displacement of the upper shock by about 2 mm and a slight upward shift in the turbulent wake. This is as expected and indicates a slightly weaker separation for the oscillatory flow.

Animation-frame displays of the oscillatory pressure and turbulent energy fields are shown in figures 16 to 18 and 19 to 21 respectively. Each of these figures shows ten equally spaced frames for a single cycle of oscillation. The frames are arranged anticlockwise, starting with zero displacement at the top left. Each frame shows the instantaneous oscillatory field, together with the value of the generalised coordinate, $q(t)$, and a bar indicating the vertical displacement of the bump surface.

In all these displays, the time variation of the field is predominantly at the fundamental surface frequency, with the main difference between the three frequency cases being in the relative phase. Caution must be exercised in interpreting any apparent higher frequency variations, due to the relatively coarse 'frame rate' used. Any fluctuations which have frequencies above five times that of the surface oscillation will either be completely invisible here, or will appear as noise at lower 'aliased' frequencies.

The field pressure displays, 16 to 18, may be compared with the corresponding surface pressure diagrams, 9 to 11. The pressure variations in the two displays, at and near the surface, are consistent. For the 10 Hz and 100 Hz cases, the pressure oscillation, of the order 15 kPa, is tightly confined to the shock and is in phase with that at the bump surface. For the 500 Hz case however, whilst still dominated by the shock, the pressure variation is much more widely spread, with an amplitude of about 1.6 kPa near the tunnel ceiling, directly above the bump.

The turbulent energy displays, 19 to 21, all show behaviour consistent with a small vertical displacement of the wake origin, the separation bubble, at the same frequency as the surface oscillation. For the 10 Hz and 100 Hz cases, the oscillation is so slow that any disturbance in the wake is swept down its full length within the time interval of a single frame. However, at 500 Hz, the wavelength of such a disturbance is small enough for oscillations in the wake to be clearly seen. There is marked variation in the phase of the wake disturbance relative to the surface motion. The magnitude is however, less strongly frequency-dependent, decreasing only by about a factor of three over the range 10 Hz to 500 Hz.

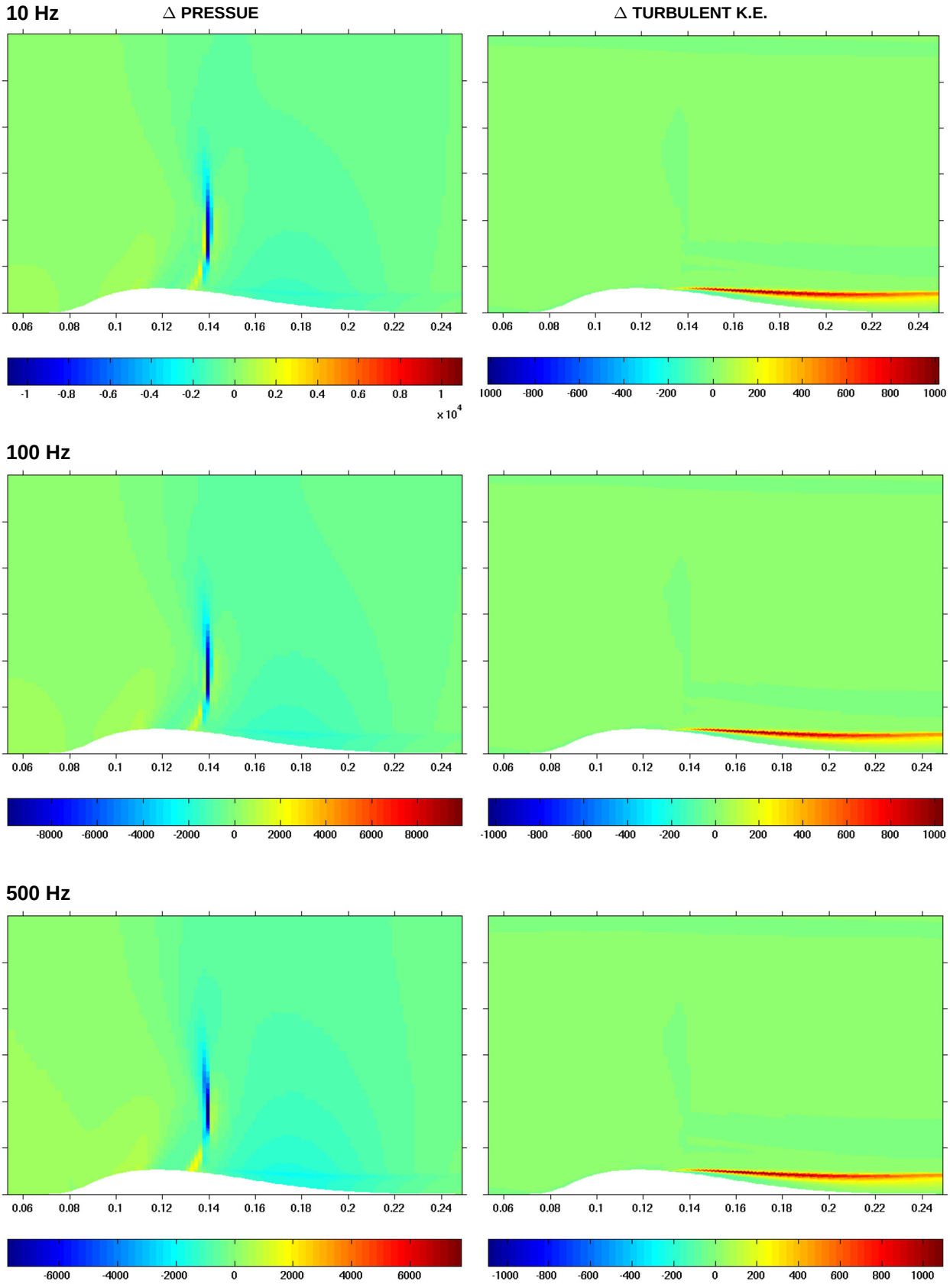

Figure 15. Differnece Mean - Steady for Pressure and Turbulent Energy

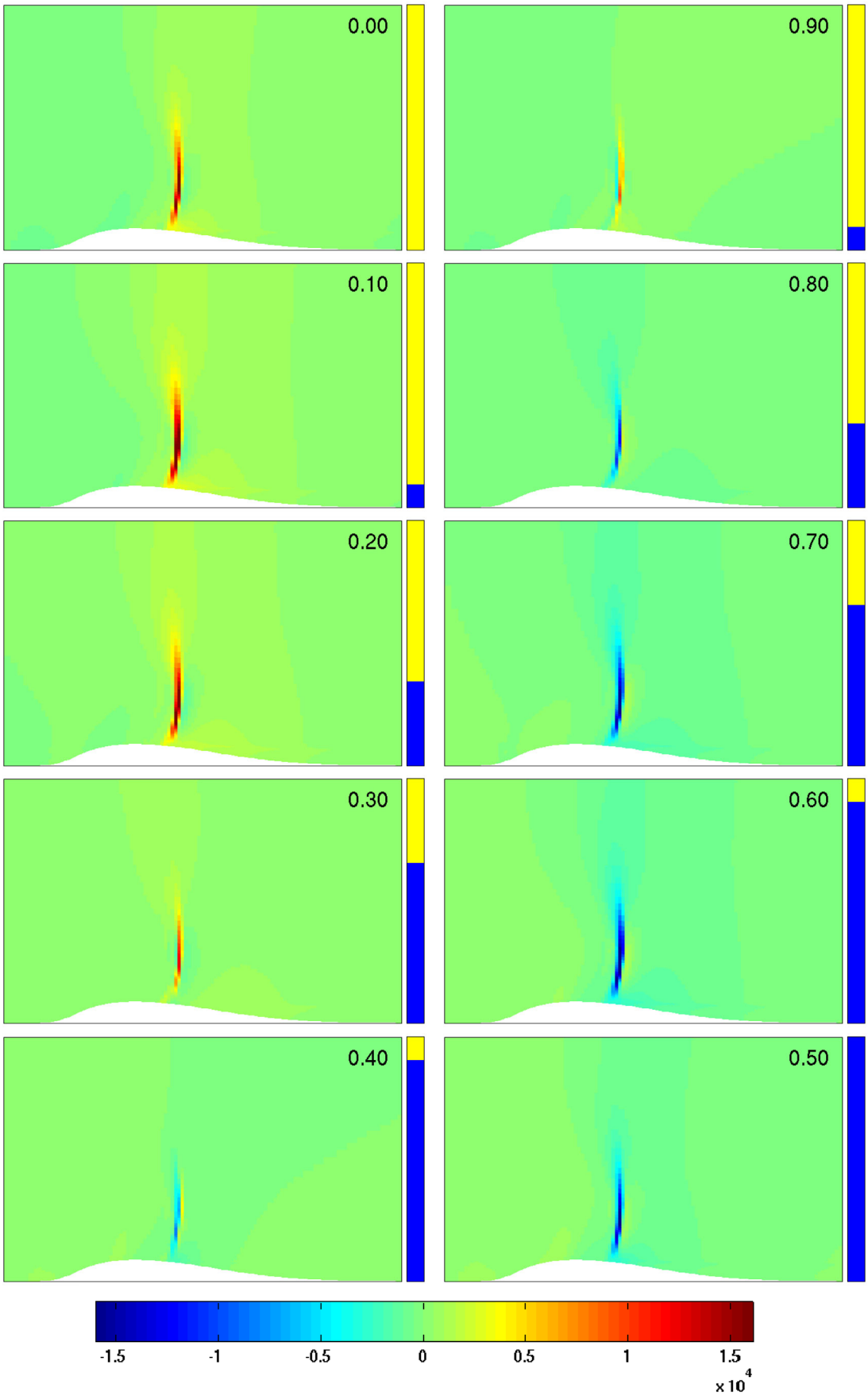

Figure 16. Animation frame cycle: unsteady Pressure: 10 Hz

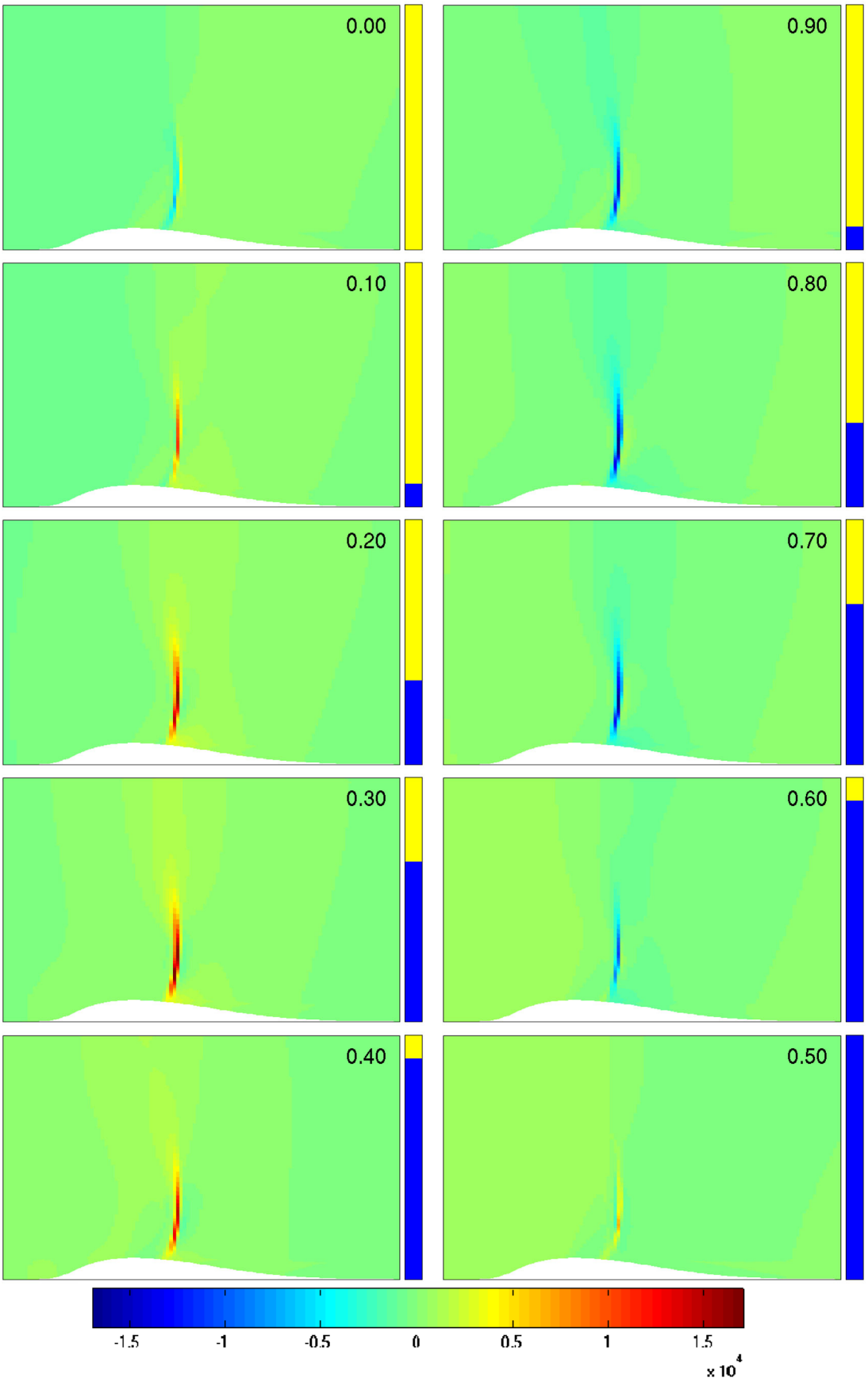

Figure 17. Animation frame cycle: unsteady Pressure: 100 Hz

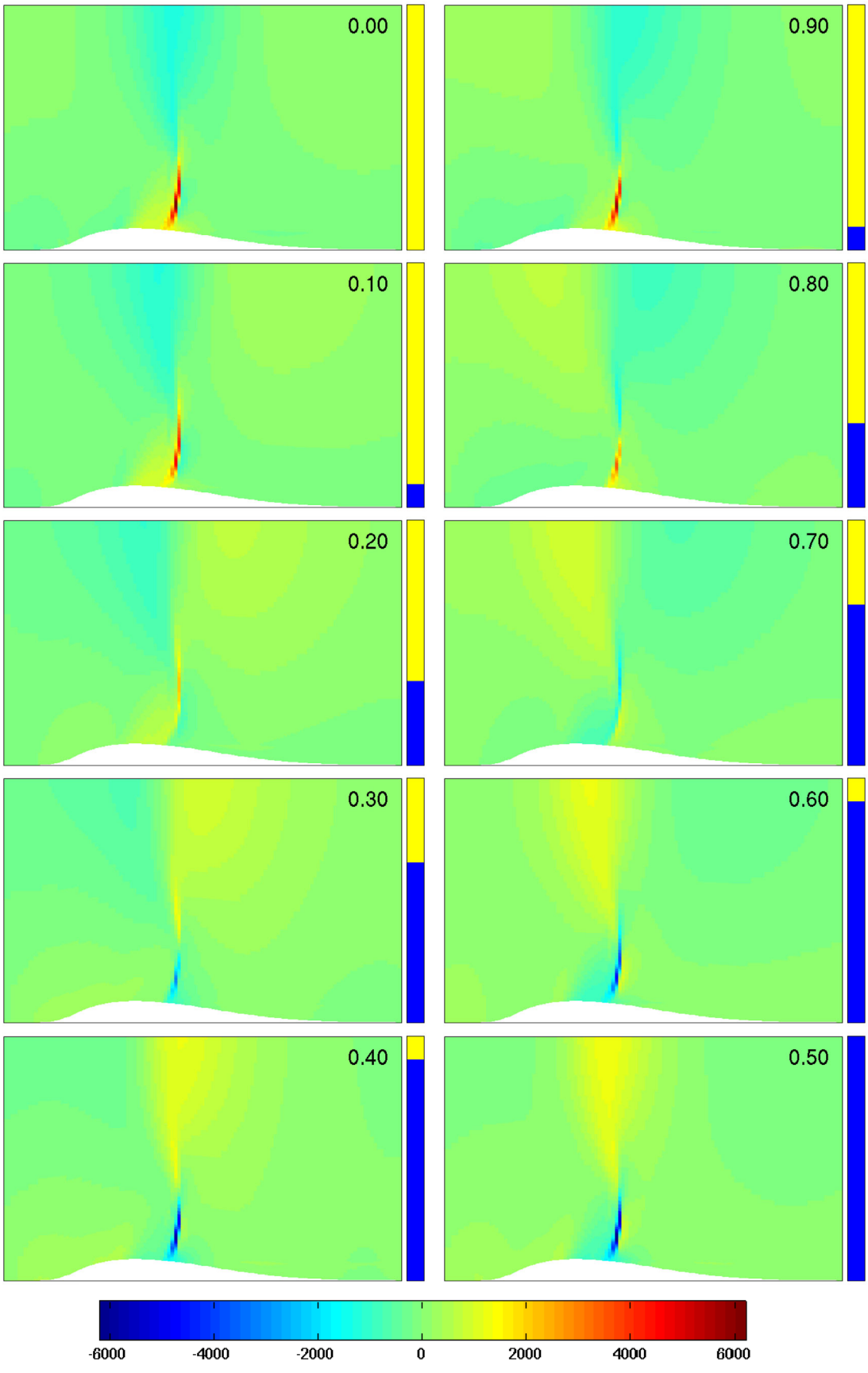

Figure 18. Animation frame cycle: unsteady Pressure: 500 Hz

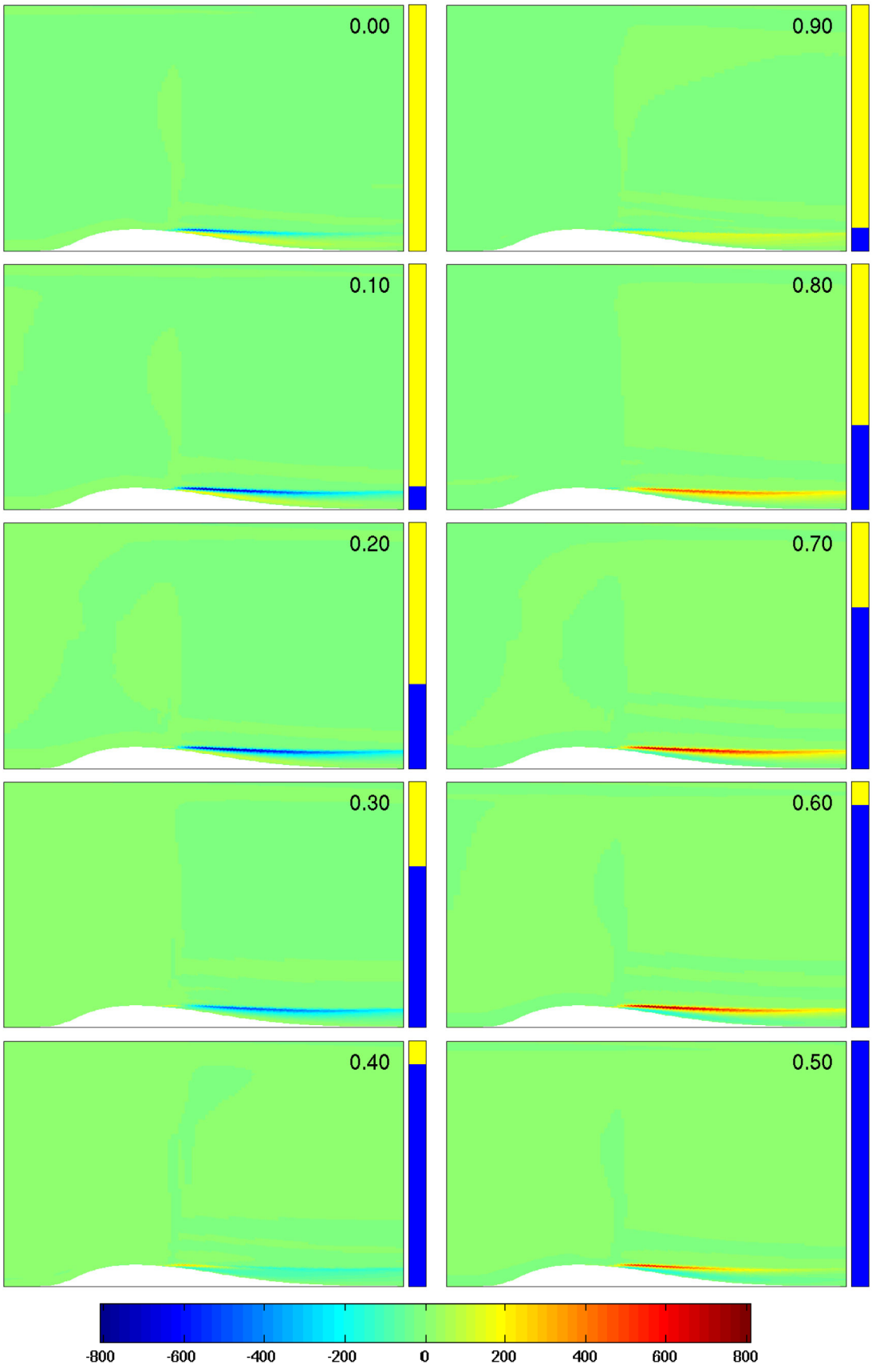

Figure 19. Animation frame cycle: unsteady Turbulent Energy: 10 Hz

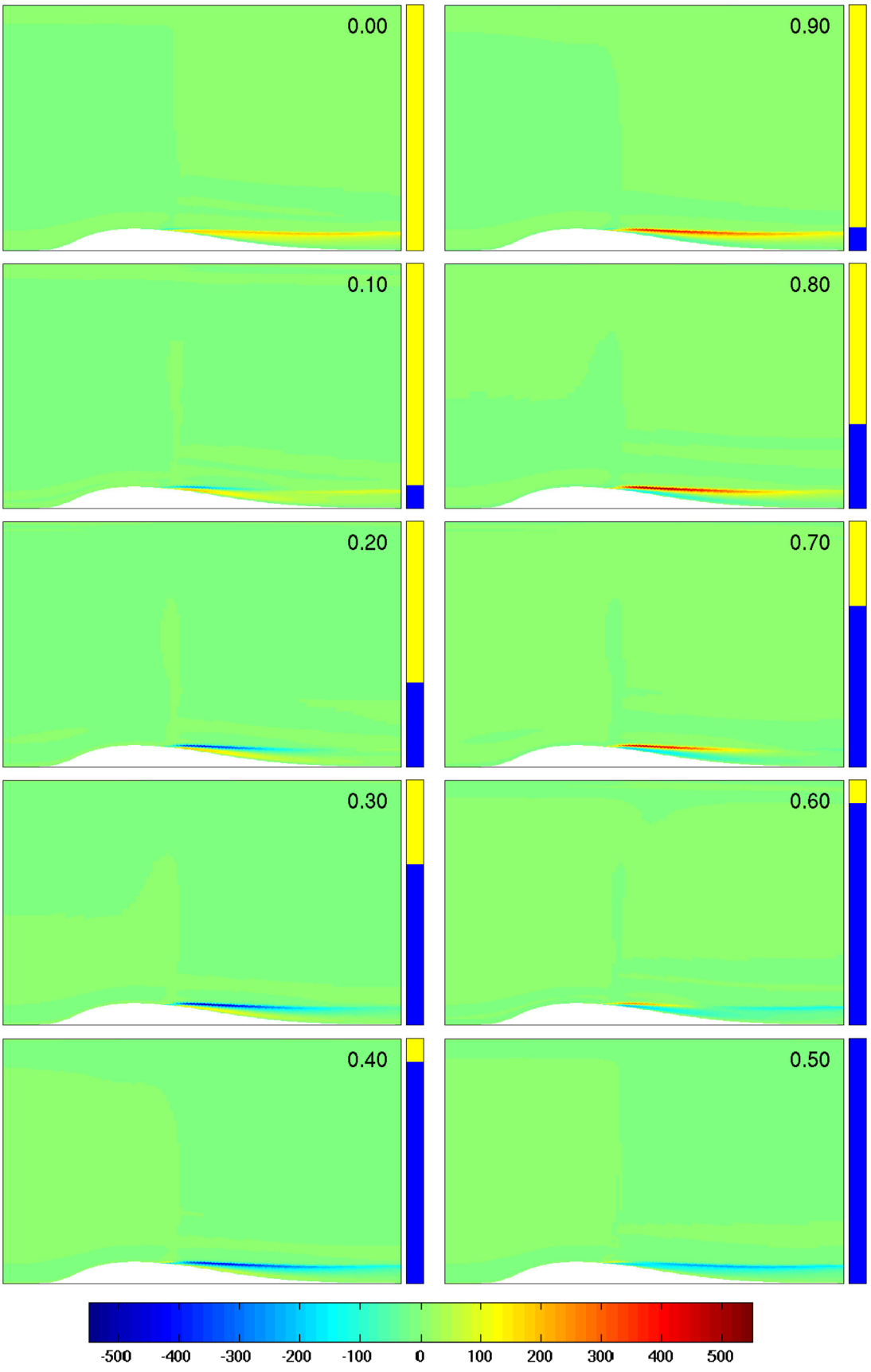

Figure 20. Animation frame cycle: unsteady Turbulent Energy: 100 Hz

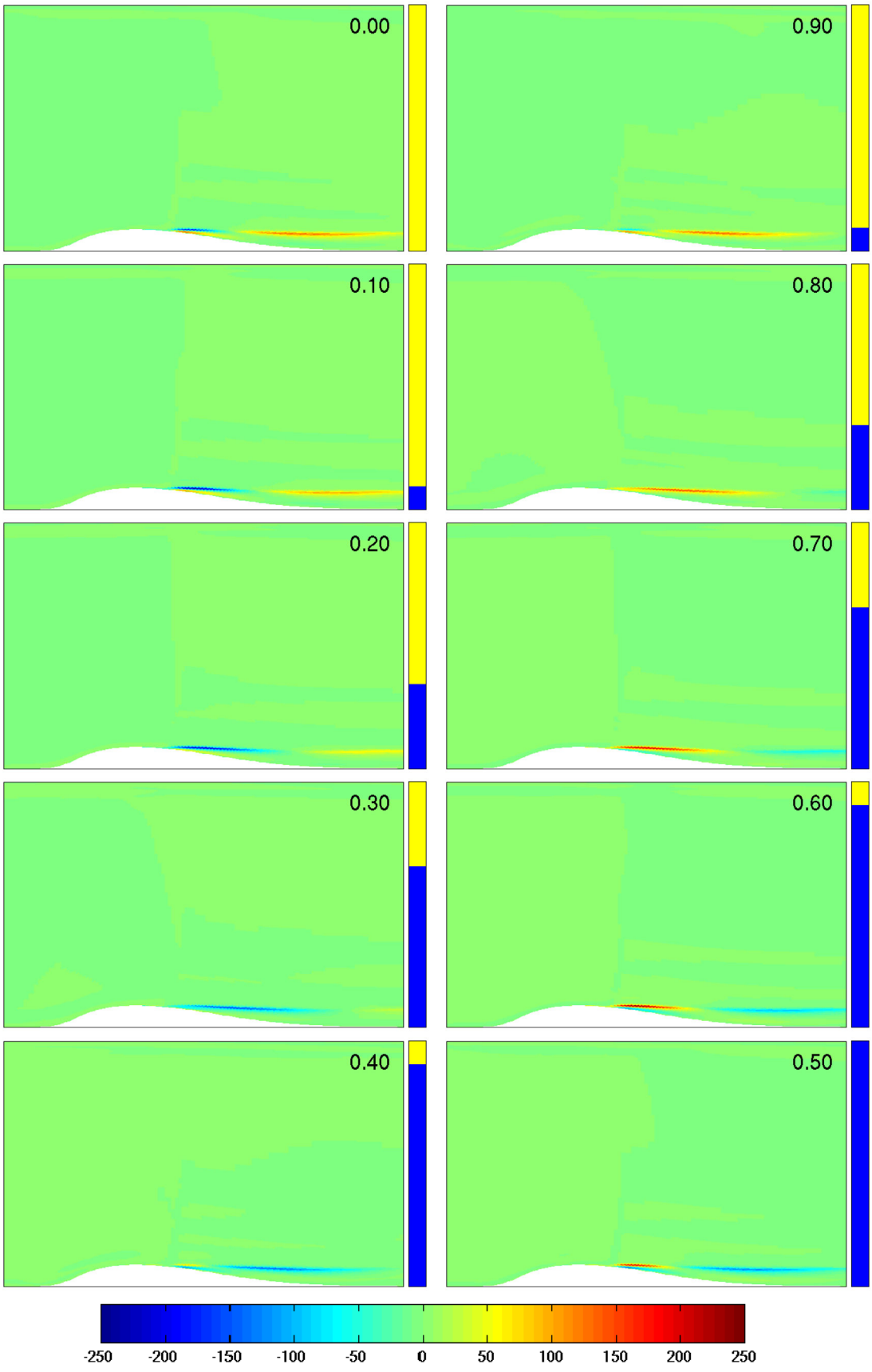

Figure 21. Animation frame cycle: unsteady Turbulent Energy: 500 Hz

3.2.5 Field Variables: Fourier Analysis

The results of Fourier analysis of the pressure and the turbulent energy fields are shown in figures 22 to 24 and 25 to 27 respectively. Each figure shows the first five 'harmonic field' components in magnitude-phase form as described in section 2.2. The field magnitude and phase variables are as defined in equation 4 and are plotted as colour contours. The colour scale for magnitude runs from zero at the centre of the colour bar (light blue) to the field maximum (red). The colour scale for phase is cyclic, centered on zero (light blue) with red denoting $\pm\pi$ radians. Each magnitude plot is labelled with the 'harmonic' frequency multiple and the maximum field magnitude for the shown region. These peak magnitude values are collected in table 4.

In contrast to the animation-frame displays in figures 16 to 21, these results are computed at the full time resolution of the solution. In the discrete-time form of equations 4 and 5, the summation over Fourier components is truncated at $n = \frac{T}{2\Delta t}$, half the number of timesteps per period of the surface oscillation. There are thus 50 components for the 10 Hz case and 25 for the 100 and 500 Hz cases. However, the results shown here are restricted to the first five oscillatory components, for which the time-resolution is ten points per cycle or higher.

Table 4. Peak magnitude of Pressure and Turbulent Energy fields from Fourier analysis of the 'working section' region.

	Pressure / $\mathrm{N\,m^{-2}}$			Turbulent Energy / $\mathrm{m^2 s^{-2}}$		
	10 Hz	100 Hz	500 Hz	10 Hz	100 Hz	500 Hz
H1	2.06e4	1.88e4	6.61e3	8.45e2	5.74e2	2.55e2
H2	5.80e3	4.05e3	6.00e2	7.53e1	5.47e1	9.61e0
H3	3.14e3	2.05e3	7.38e1	2.52e1	1.12e1	3.32e0
H4	5.40e2	3.19e2	1.32e1	6.24e0	3.50e0	1.50e0
H5	5.01e2	2.29e2	1.34e1	4.23e0	2.48e0	1.11e0

For the 'first harmonic' fields, denoted 'H1', the phase is simply related to the surface motion. Referring to equations 4 and 2, it can be seen that the field is in phase with the bump surface displacement when the phase angle, ϕ, is $\pm\pi$ (red) whilst $\phi = 0$ (light blue) corresponds to the antiphase, 'bump down, field up', state. For the higher harmonics, the phase variable may be interpreted in a similar fashion, referring to a notional surface oscillation at the multiple frequency.

Referring to table 4, it can be seen that for all three frequency cases, both fields are dominated by the response at the driving frequency, H1. The H1 peak magnitude is typically about ten times larger than the H2 value. This observation is consistent with the Fourier analysis of the surface pressures in section 3.2.3 and the time domain display in section 3.2.4.

The pressure fields shown in figures 22 to 24 confirm the observations made in section 3.2.4 but provide a much more detailed presentation of the time dependent structure of the field. The pressure magnitude plots show clearly how the spatial spread of the unsteady pressure increases with frequency. The phase information has a less direct physical significance but it appears to be a very sensitive indicator of other structures in the flow. For example, the pressure phase for components, H3 to H5 show the same 'source and wake' pattern as in the steady turbulent viscosity, figure 5. Similarly, the wake in the turbulent energy is indicated in the H2 phase at 10 Hz and the H1 phase at 100 Hz. The phase distribution for the H1 components is smooth and continuous throughout the field. However, for the

higher components, there is an apparent loss of coherence in some areas. This is most noticeable in the lower shock region.

The turbulent energy fields are shown in figures 22 to 24. As with the pressure data, these images are consistent with the time domain presentation but they reveal much more detailed structure in the flow. The magnitude plots show clearly the main turbulent wake from the separation bubble but also wakes starting higher up on the shock line. These features are strongest in the 10 Hz and 100 Hz cases. The phase distribution is smooth and mostly continuous for the H1 components. However, there appears to be a gradual loss of coherence as the frequency index increases, with the introduction of sharp vertical discontinuities between streamwise layers. This is most pronounced in the 500 Hz case. All the phase plots show a streamwise ‘step’ in the vicinity of the shock line. This behaviour is similar to that of the unsteady pressure phase.

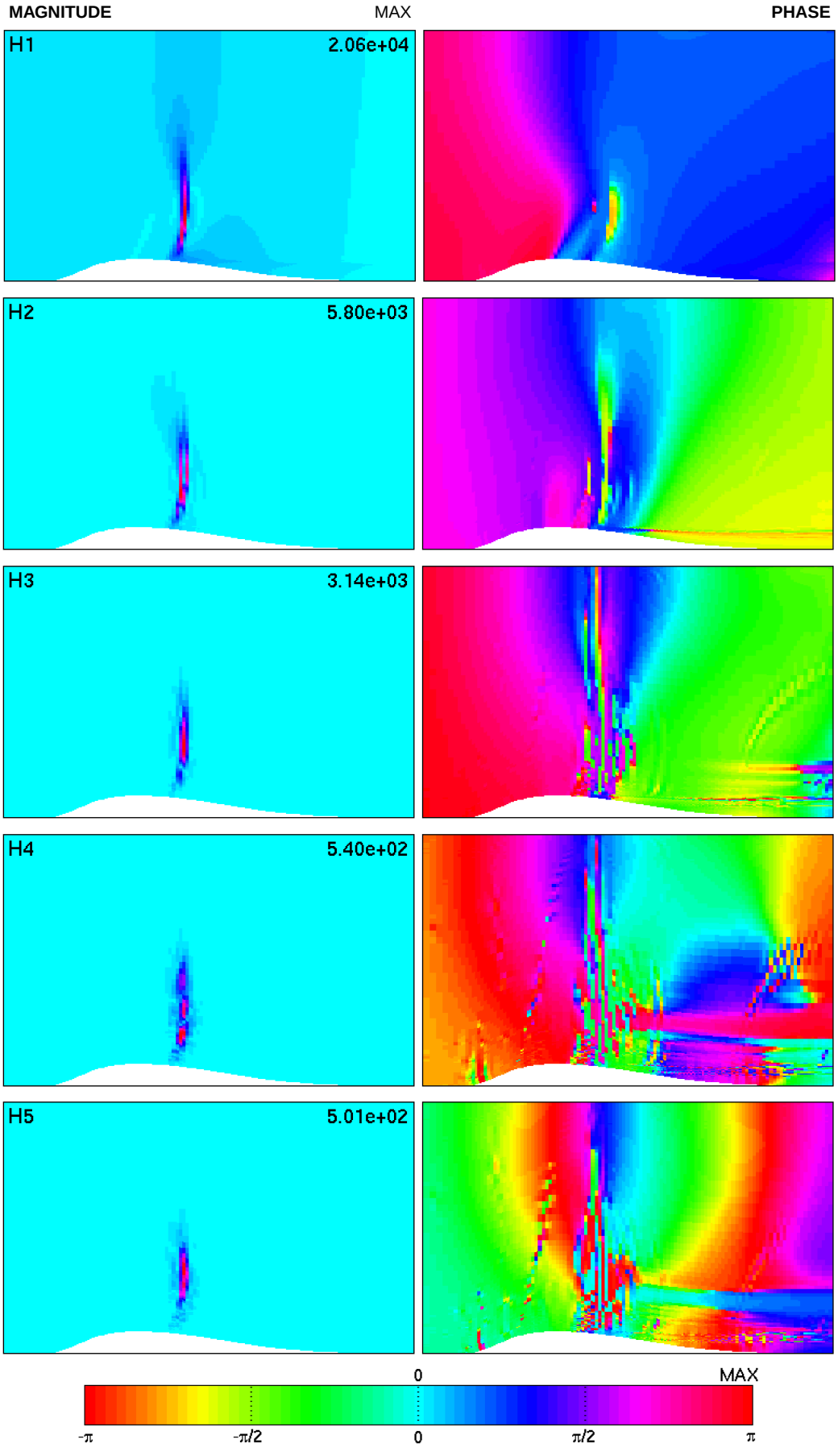

Figure 22. Fourier analysis of unsteady Pressure: 10 Hz

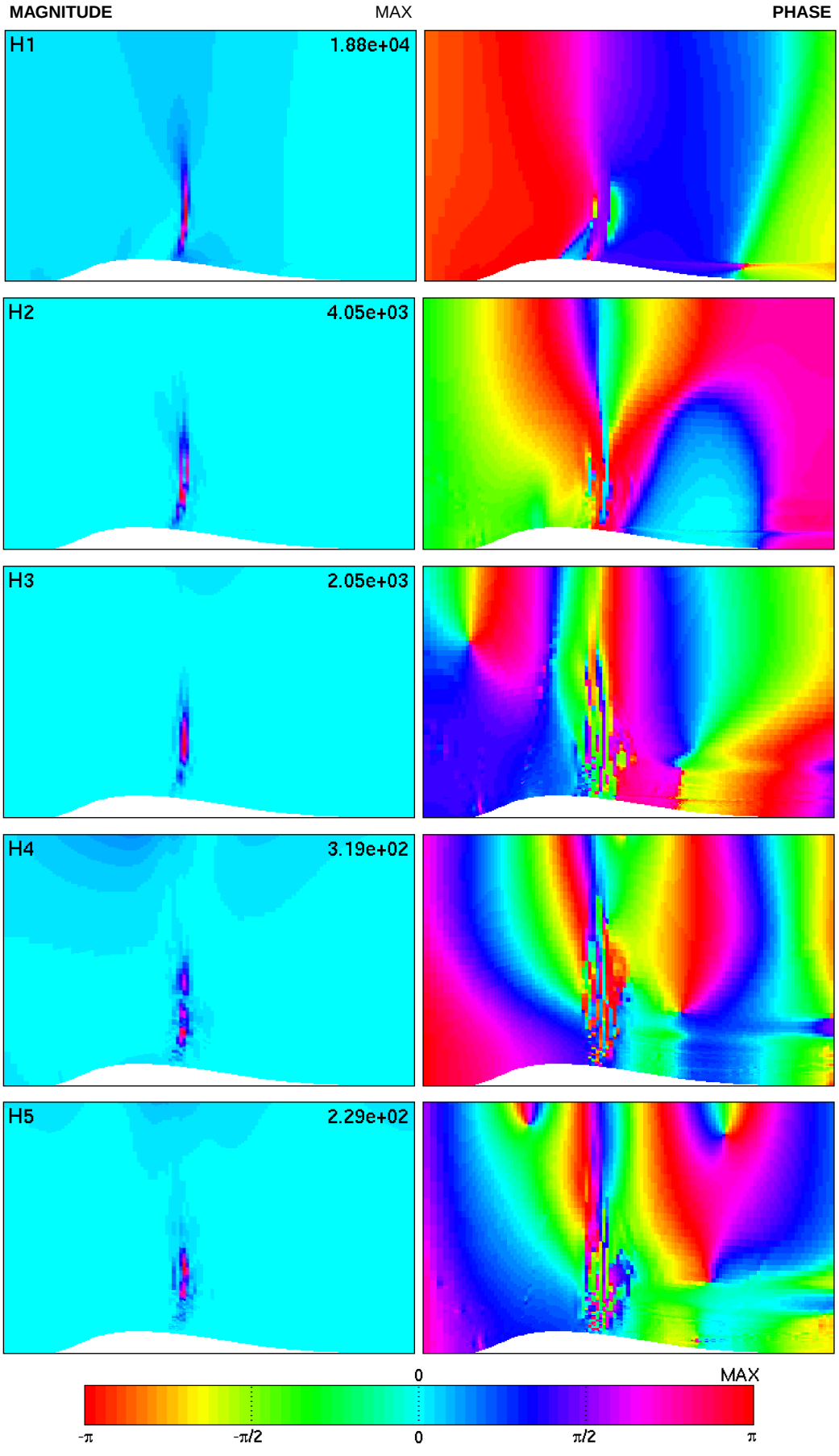

Figure 23. Fourier analysis of unsteady Pressure: 100 Hz

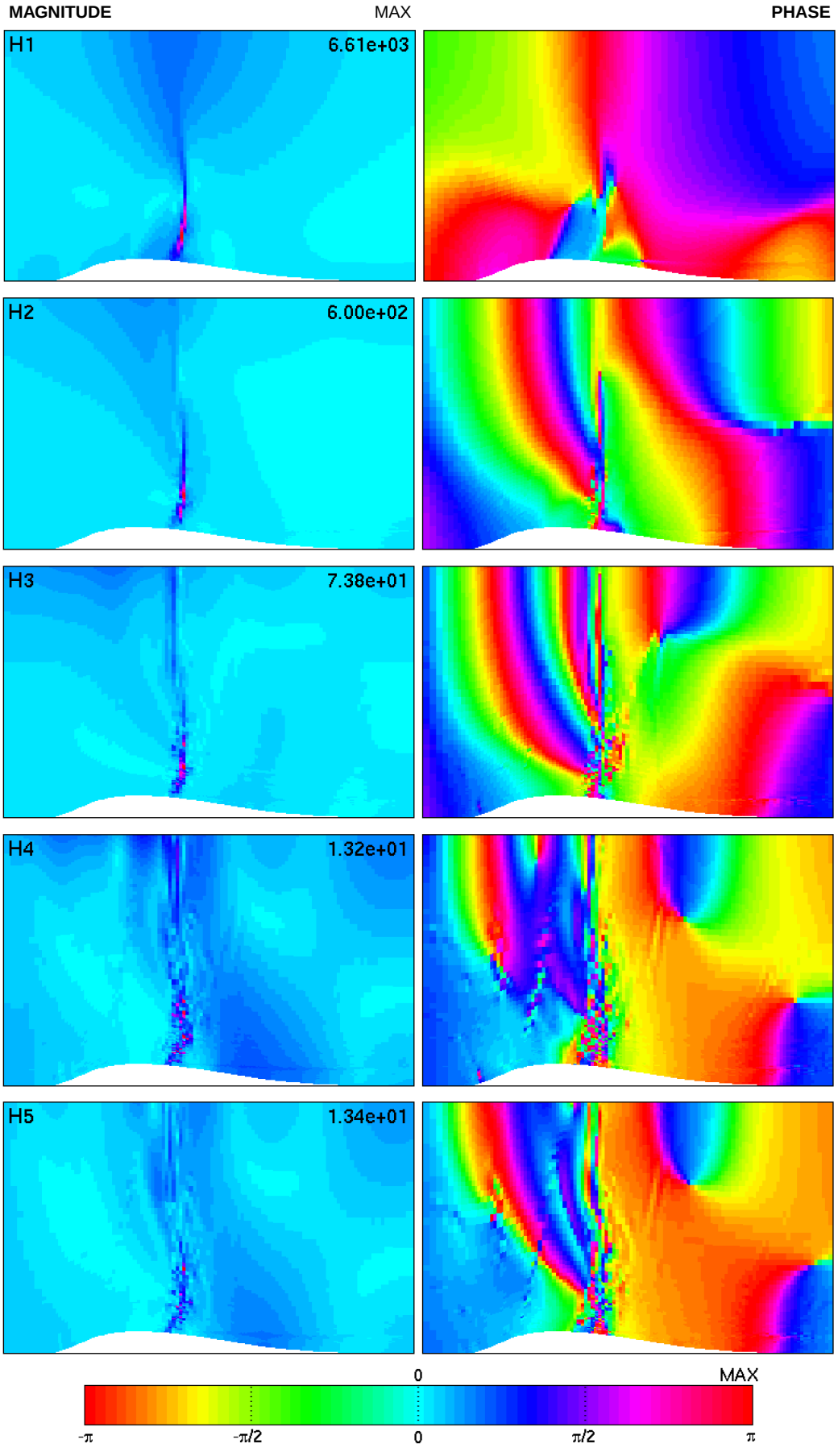

Figure 24. Fourier analysis of unsteady Pressure: 500 Hz

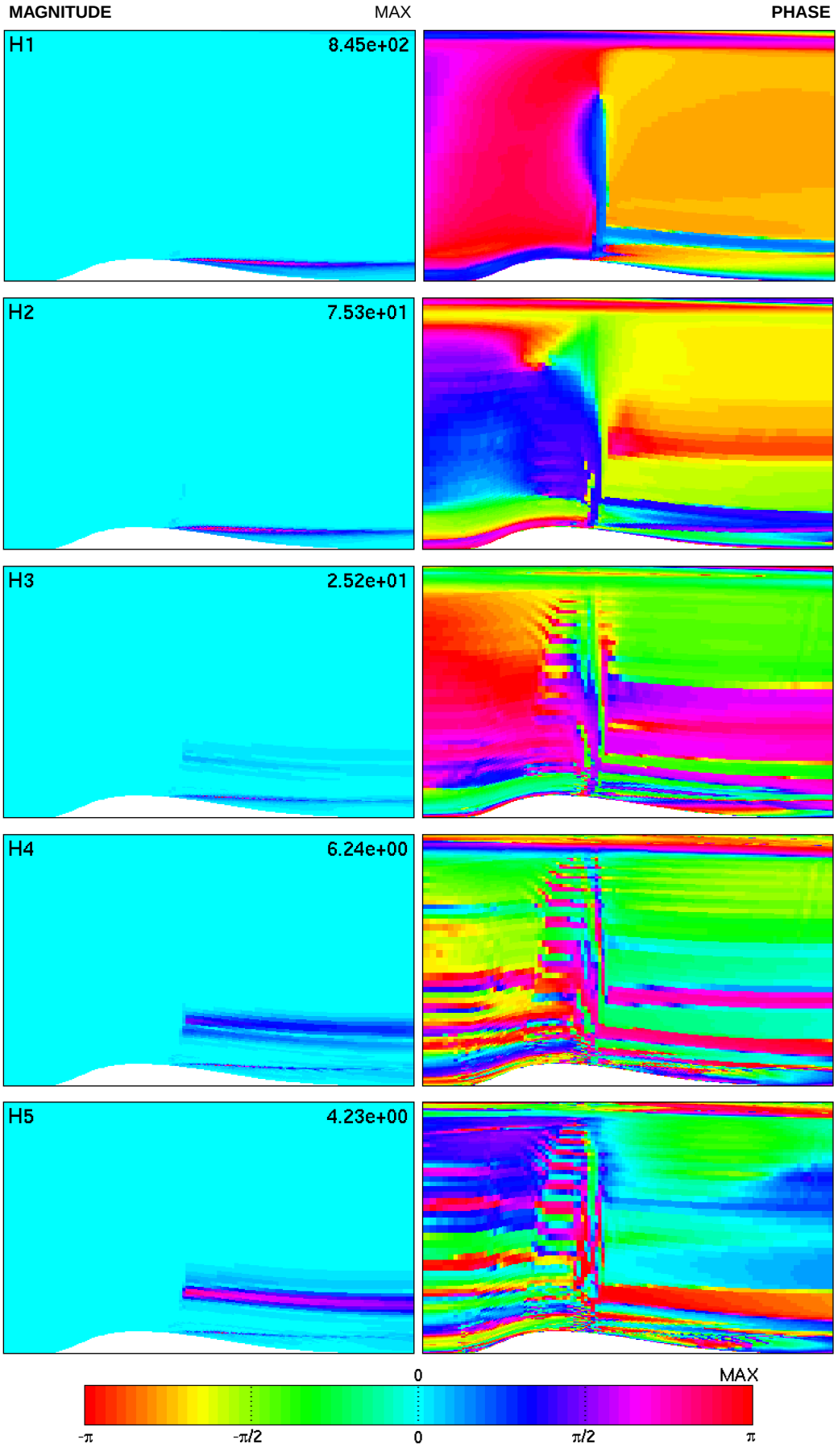

Figure 25. Fourier analysis of unsteady Turbulent Energy: 10 Hz

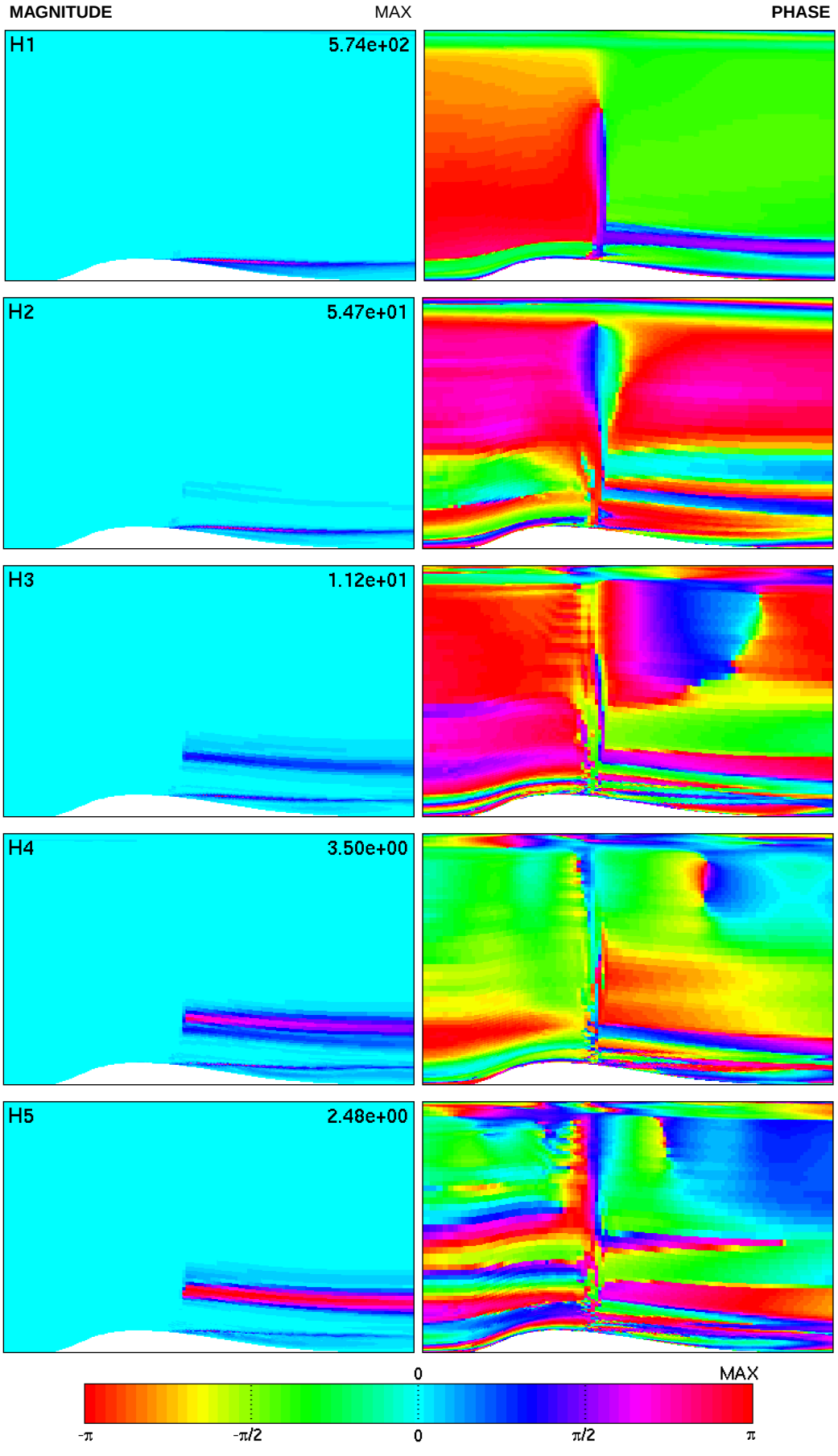

Figure 26. Fourier analysis of unsteady Turbulent Energy: 100 Hz

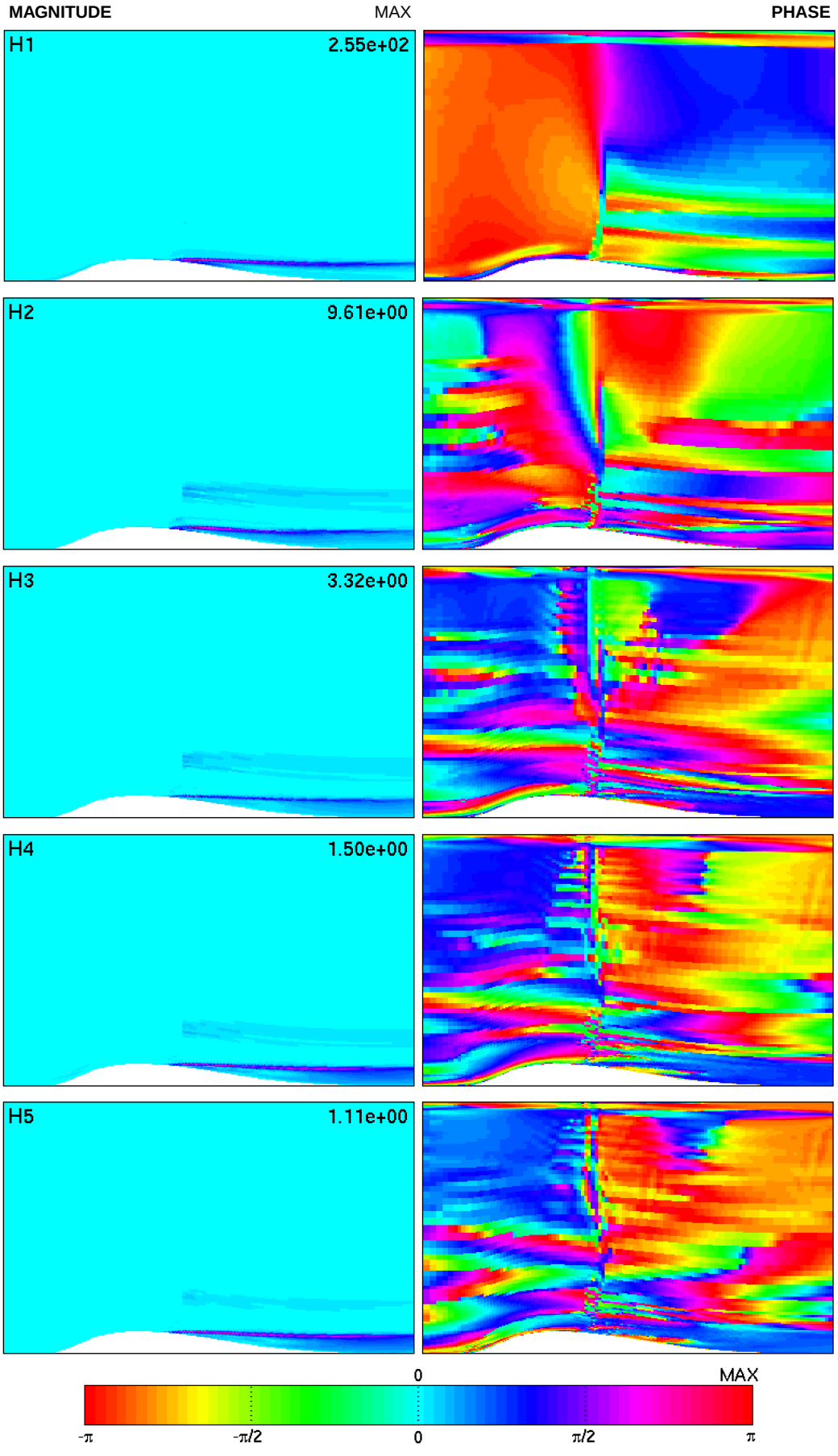

Figure 27. Fourier analysis of unsteady Turbulent Energy: 500 Hz

4 Conclusions

Results have been presented for a two-dimensional unsteady RANS calculation on the GFSI bump. These calculations are based on simple boundary data for the wind tunnel flow and an arbitrary, assumed modeshape for the surface displacement. The results are therefore only indicative of the expected behaviour of the system. For quantitative comparison with the experiment, a more detailed study will be required, based on the measured system data.

Of the predictions presented here, those which are most verifiable are for the unsteady surface pressure. These results have been presented as space-time contours and as Fourier series. In addition, detailed images have been produced for the two-dimensional unsteady pressure and turbulent energy fields. Of these results, the unsteady field pressures could be validated against measurements from pressure transducers mounted in the ceiling of the tunnel.

Fourier analysis of unsteady CFD solutions is usually restricted to the surface pressure. The analysis of the field data presented here has revealed a wealth of detailed structure. However, the physical interpretation of this data is rather challenging. The loss of coherence and discontinuities in the phase, as noted in section 3.2.5, indicate non periodic variation in the field. This would occur if the solution had poor ‘cyclic convergence’, as noted in section 3.2.1. There is also a marked difference in the coherence of the pressure and turbulent energy fields at higher frequencies. The origin of these effects requires further investigation.

The results for both surface and field pressure, show that spatial spread of the oscillatory flow increases sharply with increasing frequency. This can be understood in terms of the reduced wavelength, as described in section 2.1. It is also worth noting that, for the given free stream conditions, the fundamental ‘half-wave pipe’ frequency for the tunnel height is about 145 Hz. As shown in figures 22 to 24, the oscillatory pressure field starts to spread out even at 100 Hz, whilst at 500 Hz, there are strong pressure waves filling the whole ‘working section’ region. This suggests that in the three dimensional system, at frequencies above about 100 Hz, there could be significant interference with pressure waves reflected from the side-wall boundaries. Such effects could dramatically alter the unsteady flow field, even in the central vertical plane.

This preliminary study has established a consistent procedure for 2D computation of unsteady flow for the GFSI moving-bump. It would be relatively simple to generate further solutions, using measured data for the bump surface modeshapes and other system parameters. This would provide a set of verifiable CFD predictions for the oscillatory flow in the central vertical plane. Whilst this would be a reasonable next step, the results shown here indicate that it will also be necessary to extend the simulation to 3D. Using the same code and computing platform, this would probably require run times of several months per solution. However, using a fully parallel code, such as the FFA-developed, hybrid-unstructured solver EDGE [11] [12], the required 3D simulations should be quite feasible.

References

[1] Department of Energy Technology, KTH, `www.energy.kth.se`

[2] Swedish Energy Agency, `http://www6.stem.se/`

[3] Swedish Defence Materiel Administration, `www.fmv.se`

[4] EURANUS 5.2 User Guide (2000) FOI.

[5] Berggren M. (1998) ‘Geometric Conservation for Structured Moving Meshes’, FFA-TN 1998-28

[6] Jameson A., Schmidt W., Turkel E., (1981) ‘Numerical Solutions of the Euler Equations by Finite Volume Methods using Runge-Kutta Time-Stepping Schemes’, AIAA-81-1259.

[7] Wallin, S. & Johansson, A.V. (2000) ‘An explicit algebraic Reynolds stress model for incompressible and compressible turbulent flows.’ J. Fluid Mech. Vol. 403, pp. 89-132.

[8] Thompson J.F. (1984) ‘Grid generation Techniques in Computational Fluid dynamics’, AIAA Journal, Vol.22, No.11

[9] Tysell L.G. & Hedman S.G., (1988) ‘Towards a general three-dimensional grid generation system’, ICAS-88-4.7.4

[10] FFA Matlab Toolbox 1.4, User Manual (2002) FOI.

[11] Elliasson P. (2001) ‘EDGE, a Navier-Stokes Solver for Unstructured Grids’, FOI-R-0298-SE.

[12] EDGE 2.3 User Guide (2002) FOI.

Issuing organisation
FOI – Swedish Defence Research Agency
Division of Aeronautics, FFA
SE-172 90 STOCKHOLM

Report number, ISRN
FOI-R--0814--SE

Report type
Scientific report

Month year
Feb 2003

Project number
E840311

Customers code
3. Flygteknisk forskning

Research area code
7. Vehicles

Sub area code
79. Interdisciplinary Projects regarding Vehicles

Author(s)
Jonathan Smith

Project manager
Jonathan Smith

Approved by
Bengt Winzell
Head, Computational Aerodynamics Department

Scientifically and technically responsible
Jonathan Smith

Report title
Unsteady RANS calculations for the GFSI bump
Preliminary study using EURANUS 5.3

Abstract
Calculations are presented for unsteady transonic flow over an oscillating bump. The flow field is computed using unsteady RANS method using the FFA-developed CFD code EURANUS with the EARSM turbulence model. Flow solutions are presented in the time domain and as Fourier series. The results comprise preliminary predictions for experiments to be carried out at the Department of Energy Technology, KTH, Stockholm.

Keywords
Unsteady Aerodynamics, Energy Technology, Fluid-Structure Interaction, EURANUS, RANS, STEM

Further bibliographic information

ISSN
1650-1942

Pages
59

Language
English

Price
Acc. to price list

Security classification
Open

Utgivare	Rapportnummer, ISRN	Klassificering
Totalförsvarets Forskningsinstitut – FOI Avdelningen för Flygteknik, FFA SE-172 90 STOCKHOLM	FOI-R--0814--SE	Vetenskaplig rapport
	Månad år Feb 2003	Projektnummer E840311
	Verksamhetsgren 3. Flygteknisk forskning	
	Forskningsområde 7. Bemannade och obemannade farkoster	
	Delområde 79. Breda projekt inom farkoster	
Författare Jonathan Smith	Projektledare Jonathan Smith	
	Godkänd av Bengt Winzell Chef, Institutionen för beräkningsaerodynamik	
	Tekniskt och/eller vetenskapligt ansvarig Jonathan Smith	

Rapporttitel

Instationära RANS beräkningar för GFSI bump fallet
Preliminär studie med koden EURANUS 5.3

Sammanfattning

Beräkningar presenteras för instationär transonisk strömning över en oscillerande bula. Strömfältet beräknas med en instationär RANS metod och de av FFA utvecklade CFD-koden EURANUS samt turbulensmodellen EARSM. Strömlösningar presenteras i tidsdomän och som Fourierserier. Resultaten utgör preliminära förutsägelser av experiment som kommer att utföras vid Institutionen för Energiteknik, KTH, Stockholm.

Nyckelord

instationär aerodynamik, energiteknik, EURANUS, RANS, STEM

Övriga bibliografiska uppgifter

ISSN	Antal sidor	Språk
1650-1942	59	Engelska
Distribution enligt missiv Distribution	Pris Enligt prislista	
	Sekretess Öppen	